J. Mol. Biol. (1995) **245**, 151–179

JMB

Structural and Mechanistic Analysis of Two Refined Crystal Structures of the Pyridoxal Phosphate-dependent Enzyme Dialkylglycine Decarboxylase

Michael D. Toney[1], Erhard Hohenester[1], John W. Keller[2] and Johan N. Jansonius[1]*

[1]*Department of Structural Biology, Biozentrum University of Basel Klingelbergstrasse 70 CH-4056 Basel, Switzerland*

[2]*Department of Chemistry University of Alaska at Fairbanks, Fairbanks, AK 99775, U.S.A.*

**Corresponding author*

Two refined structures, differing in alkali metal ion content, of the bifunctional, pyridoxal phosphate-dependent enzyme dialkylglycine decarboxylase (DGD) are presented in detail. The enzyme is an α_4 tetramer, built up as a dimer of dimers, with a subunit molecular mass of 46.5 kDa. The fold of DGD is similar to those of aspartate aminotransferase, ω-amino acid aminotransferase and tyrosine phenol-lyase. The structure has two binding sites for alkali metal ions. DGD with potassium in site 1 (near the active site) and sodium in site 2 (at the surface of the molecule) has been refined against 2.6 Å resolution data (*R*-factor = 17.6%), and DGD with sodium at both sites has been refined against 2.1 Å resolution data (*R*-factor = 17.8%). The proximity of site 1 to the active site accounts for the dependence of enzyme activity on potassium ions, and the observed active site structural changes caused by ion exchange at this site explain the inhibition of activity by sodium. DGD catalyzes both the decarboxylation of dialkylglycine species and the transamination of L-amino acids in its normal catalytic cycle. The active site structure of DGD is moderately homologous to that of aspartate aminotransferase, which catalyzes only transamination; both the differences and similarities provide mechanistic guidelines for the DGD-catalyzed reactions. Models of the L-isovaline and L-alanine external aldimine intermediates suggest mechanisms by which the decarboxylation and transamination reactions could be accomplished within the single active site. Decarboxylation is proposed to be at least partially catalyzed by stereoelectronic activation of the C^{α}-carboxylate bond achieved by orienting this bond perpendicular to the plane of the pyridinium ring in the dialkylglycine external aldimine intermediate. Transamination is proposed to be catalyzed by a similar effect on the C^{α}-H bond of the L-amino acid external aldimine intermediate, combined with general base catalysis provided by Lys272, in analogy to the mechanism of aspartate aminotransferase.

Keywords: dialkylglycine decarboxylase; pyridoxal-5'-phosphate; X-ray crystallography; enzyme mechanism; alkali metal ion binding sites

Introduction

Dialkylglycine decarboxylase (DGD; EC 4.1.1.64) is an unusual pyridoxal phosphate-dependent enzyme that catalyzes both decarboxylation and transamination in its normal catalytic cycle (Aaslestad & Larson, 1964; Bailey & Dempsey, 1967). It is an α_4 tetramer (Lamartiniere *et al*., 1971)

Present address: M. D. Toney, Department of Biochemistry, Albert Einstein College of Medicine, Bronx, NY 10461-1602, U.S.A.

Abbreviations used: DGD, dialkylglycine decarboxylase; DGD-K^+, DGD with potassium in metal binding site 1; DGD-Na^+, DGD with sodium in metal binding site 1; PLP, pyridoxal phosphate; PMP, pyridoxamine phosphate; AAT, aspartate aminotransferase; APT, ω-amino acid aminotransferase; TPL, tyrosine phenol-lyase; PPL-Cys-Hg, *N*-(5'-phosphopyridoxyl)-*S*-methylmercuri-L-cysteine; MIR, multiple isomorphous replacement. Superscript-asterisks (*) denote residues that are contributed by the second, symmetry-related subunit in the dimer. r.m.s., root-mean-square.

0022–2836/95/020151–29 $08.00/0

with a subunit molecular mass of 46.5 kDa. The cloning and sequencing of the DGD gene from the soil bacterium *Pseudomonas cepacia* was reported by Keller *et al*. (1990), who also showed that the enzyme is related to aminotransferases rather than to classical decarboxylases. This suggests that DGD is an aminotransferase that has, through evolution, acquired decarboxylase activity rather than a decarboxylase that has acquired aminotransferase activity. The physiological role of the enzyme is not clear. 2,2-Dialkylglycines are major constituents of fungal antibiotics (Brückner & Pryzbylski, 1984), which may be a substantial carbon and fixed nitrogen source.

The catalytic cycle of DGD is composed of two half-reactions operating in a ping-pong kinetic mechanism. DGD acts on small 2,2-dialkylglycine species in the decarboxylation half-reaction, and, preferentially, pyruvate in the transamination half-reaction, e.g.:

DGD-PLP + 2-aminoisobutyrate

$$\rightarrow \text{DGD-PMP} + CO_2 + \text{acetone}$$

$$\text{DGD-PMP} + \text{pyruvate} \rightleftharpoons \text{DGD-PLP} + \text{L-alanine}$$

The decarboxylation half-reaction is different from the principal reaction catalyzed by classical decarboxylases in that the substrate amino group is obligatorily transferred to the coenzyme (i.e. oxidative decarboxylation), but is similar to the abortive side reaction that these enzymes undergo (Sukhareva, 1986).

In addition to the mechanistic peculiarity of DGD, the enzyme has been shown to be dependent on potassium ions for activity and stability (Aaslestad *et al*., 1968). In a brief report of the DGD structure (Toney *et al*., 1993), two alkali metal ion binding sites were described: one near the active site that binds a variety of alkali metal ions and regulates activity, and a second near the surface of the molecule that is specific for sodium ions. Here, we present two refined crystal structures of DGD, one with potassium and one with sodium bound near the active site. The metal binding sites are described in detail and their structures are integrated into the existing body of data on metal ion binding sites in proteins.

A mechanistic model that accounts for the observed activity of DGD towards various substrates and the ability of the enzyme to catalyze both decarboxylation and transamination *via* a single active site is proposed. This model is based on the experimentally derived Mes-liganded active site structure and model structures for the external aldimine intermediates with L-alanine and L-isovaline.

Results

Quality of the structures

Two distinct DGD native structures differing in metal ion content were refined independently. The DGD-K^+ structure contains a potassium and a sodium ion, whereas the potassium is exchanged for a second sodium ion in DGD-Na^+. Despite the differing ion content, the overall structures of the resulting models are very similar. However, the active site and metal ion binding site structures differ substantially between DGD-K^+ and DGD-Na^+. The following description of the overall structure is based on the higher resolution DGD-Na^+ structure.

The refined DGD-Na^+ model comprises 93% of the DGD molecule, 229 water molecules, a Mes buffer molecule and two sodium ions. The main-chain atoms of all residues except for the first two, and two loop segments (residues 142 to 143, and residues 367 to 376), have clearly defined electron density. The side-chains of several charged residues on the protein surface are not well defined by the electron density. Figure 1 shows the electron density for the PLP coenzyme and selected active site residues. The *R*-factor is 17.8%, based on 32,089 structure factors between 8 and 2.1 Å resolution. The final model has excellent stereochemistry and, in addition, fulfils the criteria for an accurate model suggested by Morris *et al*. (1992); namely, narrow distributions of the amino acid side-chain torsion angles (χ_1), and a narrow distribution of the hydrogen bond energies, which were calculated by the method of Kabsch & Sander (1983). The distributions of both of these quantities provide an unbiased measure of the quality of the model since they were not restrained in the refinement process. The overall error in the atomic positions, calculated by the program SIGMAA (Read, 1986), is 0.27 Å. This agrees with the estimated coordinate error of less than 0.25 Å obtained from the Luzzatti plot shown in Figure 2. A Ramachandran plot of the DGD-Na^+ model is shown in Figure 3. Refinement statistics and stereochemical parameters for the DGD-K^+ and DGD-Na^+ models are summarized in Table 6. The refined coordinates of both structures have been deposited with the Brookhaven Protein Data Bank (Bernstein *et al*., 1977); the entry codes are 1DKB and 1DKA for the DGD-K^+ and DGD-Na^+ structure, respectively.

Overall structure

DGD is known to exist as an α_4 tetramer in solution (Lamartiniere *et al*., 1971) and this quaternary structure is observed in the present crystal structures. All four monomers in the tetramer are crystallographically identical due to the coincidence of the molecular 2-fold axes with crystallographic axes. In the following, the structure is described beginning with the monomer, then moving to the dimer, and finally the tetramer. A ribbon representation of the fold of the DGD monomer is presented in Figure 4. A schematic representation of the secondary structural elements together with the nomenclature used in this paper is given in Figure 5. Table 1 lists the β-turns in DGD.

The monomer is best subdivided into three portions: (1) a large, PLP binding domain; (2) a smaller, C-terminal domain; and (3) an N-terminal

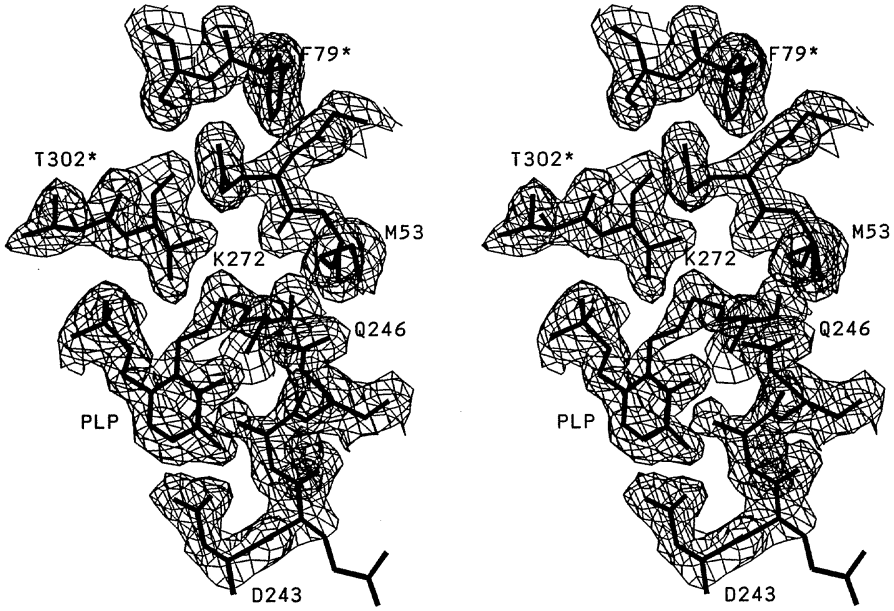

Figure 1. Stereo drawing showing the electron density of the cofactor and surrounding atoms in the active site of DGD-Na^+, with the refined model superimposed. The ($2F_{obs} - F_{calc}$), α_{calc} map was calculated at a resolution of 2.1 Å and is contoured at a level of 1.0 σ above the mean. Residues contributed by the second subunit in the dimer are labeled with an asterisk (*).

segment that includes a helix and a small, three-stranded, antiparallel β-sheet.

The central structure of the large domain is a seven-stranded β-sheet (*a, g, f, e, d, b, c*) in which six of the strands are parallel (+, –, +, +, +, +, +). This sheet is covered on both sides by eight α-helices of varying length. PLP binds near the N terminus of helix 4 and the C termini of strands *e* and *f*. A four-stranded, antiparallel β-sheet (strands *D, E, F* and *G*) in the small domain mediates the majority of its interactions with the large domain. Completing the small domain, three α-helices pack against the sheet on the side opposite that of the large domain. It is debatable whether or not to include the N-terminal segment as a part of the small domain. The distinction made here is based on their spatial separation and the relatively small number of interactions between these two structures.

Two monomers associate tightly to form a dimeric structure as shown in Figure 6. The interaction surface between the two monomers is large: 3770 $Å^2$ of solvent-accessible surface area per monomer are buried upon dimer formation. The 2-fold dimer symmetry axis passes between the C termini of helices 5 and the middles of helices 2. The active sites are close to each other (the PLP phosphate atoms are separated by 15 Å) and are ''shared'' (i.e. each is formed from residues contributed by both

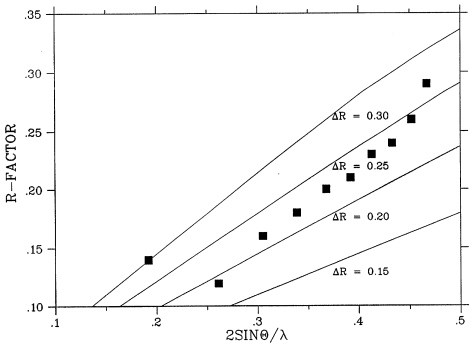

Figure 2. Variation of the *R*-factor of DGD-Na^+ with resolution (Luzzati, 1952). The overall *R*-factor is 0.178. The thin lines represent the theoretical variation of the *R*-factor with resolution, assuming coordinate errors of 0.15, 0.20, 0.25 and 0.30 Å. The mean coordinate error of DGD-Na^+ estimated from this plot is less than 0.25 Å.

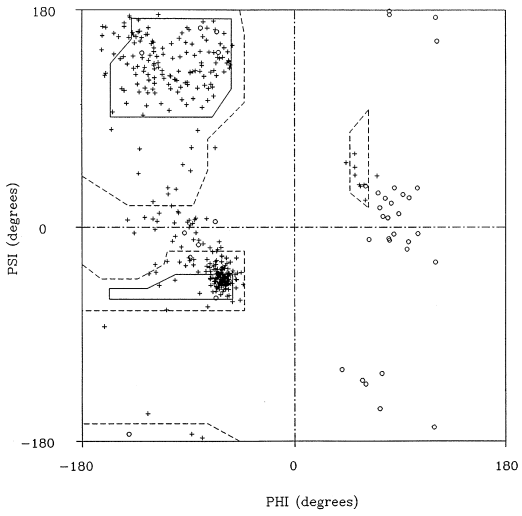

Figure 3. Ramachandran plot for DGD-Na^+. Non-glycine residues are represented by crosses, glycine residues by small spheres.

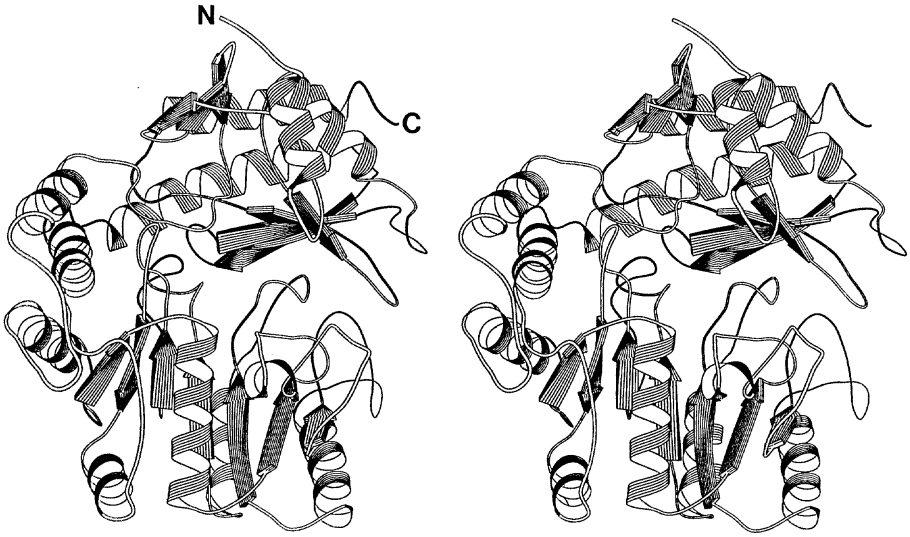

Figure 4. Stereo cartoon representation of the DGD subunit fold. The large PLP binding domain is at the bottom, the smaller C-terminal domain is at the upper right. The N and C termini are marked. Made with the program RIBBON (Priestle, 1988).

monomers in the dimer). The angle between the axes of helices 4 (the phosphate-binding helix, see below) in the dimer is approximately 90°.

Intimate contacts between the two monomers in the dimer are made by the N-terminal helix and its associated loop. This helix and loop are not only involved in numerous hydrophobic interactions with the large domain of the other monomer, but also participate in a remarkable, well-ordered cluster of charged residues in the dimer interface, where Arg20

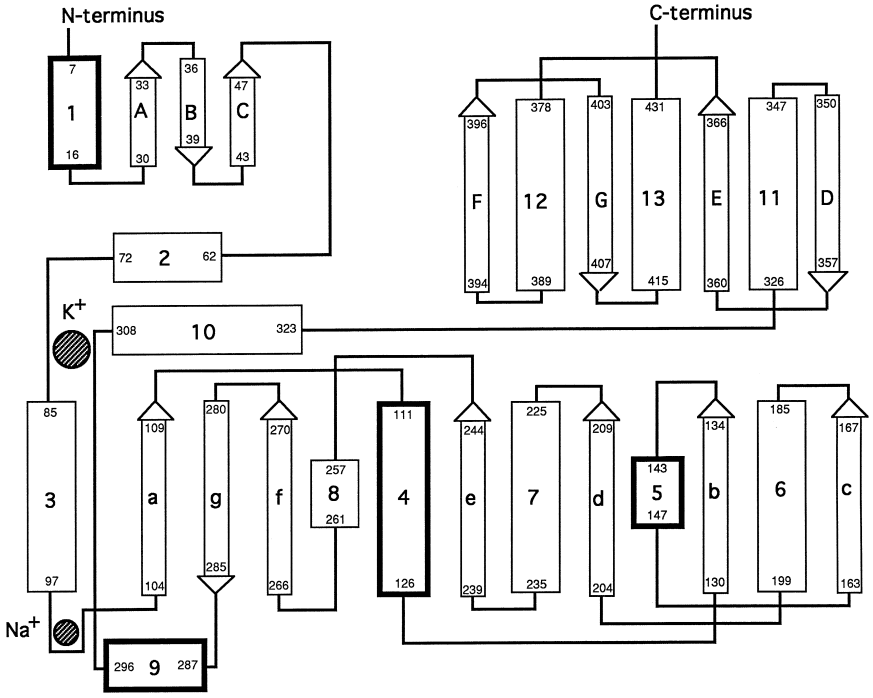

Figure 5. Schematic drawing showing the secondary structural elements in the DGD structure together with the nomenclature used in this work. Rectangular boxes in bold and thin outline represent α-helices above and below the β-sheets, respectively (in the view of this Figure; compare Figure 4). β-Strands are represented by arrows. The residue range of each secondary structural element is indicated. The approximate locations of metal binding sites 1 (K^+) and 2 (Na^+) are also given. The overall content of α-helix and β-sheet is 38% and 16%, respectively. Secondary structure definitions were made with the program DSSP (Kabsch & Sander, 1983).

Table 1

Turn types and sequence position in DGD

Residue numbers	Number of H-bonds† (i, i + 3)	Type of β-turn
33–36	1	II'
39–42	1	I
47–50	0	I
55–61	1, 0	I, II
72–75	1	I
79–82	1	I
99–102	1	II
134–137	1	I
146–149	1	I
161–164	0	II
171–174	0	I
179–182	1	I'
214–217	1	I
222–225	1	II
234–237	1	I
247–253	0, 1	II, I
275–278	1	I'
294–297	1	I
302–307	0, 0	I, II
322–325	1	I
348–351	0	I
357–360	1	II'
387–390	1	I
398–401	1	II
410–413	1	I

† A cutoff criterion of 3.2 Å was used.

interacts strongly with Arg104*, Glu290* and Glu291*. Helices 2 and 2* pack against each other with a crossing angle of ∼15°. Mostly hydrophobic residues are found in the contact region between these helices, with the exception of a salt bridge between His59 and Asp76*. The C terminus of helix 2 also hydrogen bonds to strand A of the small, N-terminal β-sheet of the adjacent subunit. This β-sheet forms a type of clamp in the triangular corner where both large domains and the small domain of one monomer make their closest approach. In the center of the dimer and near the active sites, helix 5 interacts with its symmetry mate *via* residues 142 and 143. The amide nitrogen atom of Gly143 also hydrogen bonds to the Glu116* side-chain carboxylate group, located in the phosphate-binding helix. Met141, an active site residue, packs against Phe300* of the other subunit. Pro279, situated in the short α-helical turn connecting strands *f* and *g* of the large β-sheet, is in van der Waals contact with its symmetry mate and with His304* of the other subunit. Completing the dimer interface, the loop comprising residues 159 to 162 packs against its symmetry mate and also takes part in the tetramer interface.

The tetramer (Figure 7) is formed by the symmetric association of two dimers, lending overall 222 symmetry. The tetramer interface is three times smaller than the dimer interface; only 1220 Å^2 of surface area per monomer are buried upon tetramer formation from dimers. The interface is largely formed by interactions between helix 6 and its N-terminal associated loop with their symmetry mates, and between this helix and strand *c* of the large domain β-sheet. Approximately ten residues from each subunit are involved in the formation of the tetramer interface. Val162 at the N terminus of strand *c* points into the very center of the tetramer, and Phe177 and Tyr191 pack closely with their symmetry mates. Several hydrogen bonds, as well as a water-mediated salt bridge (Arg196 with Asp194*) also contribute to the interface.

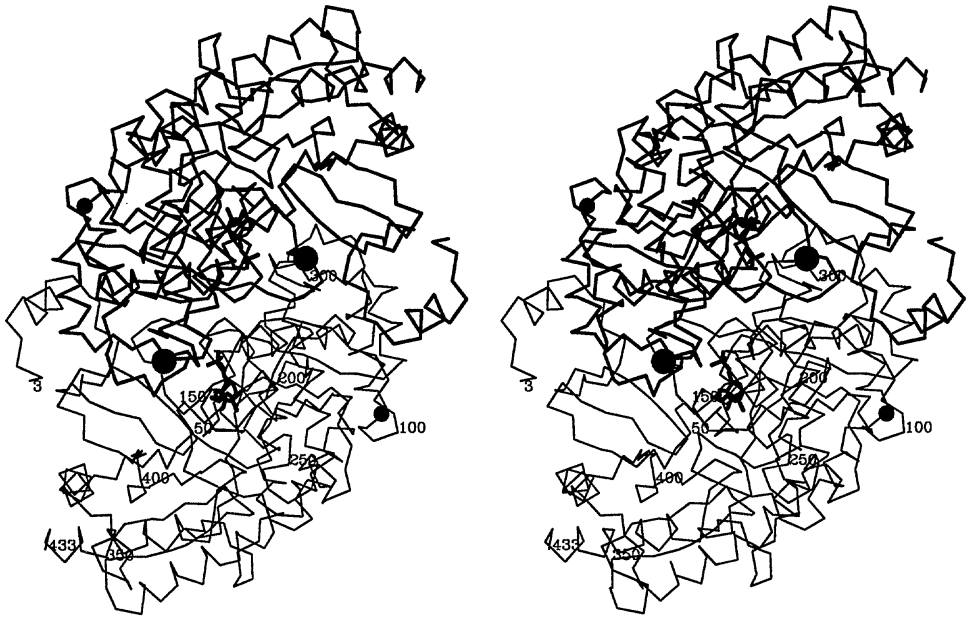

Figure 6. α-Carbon stereo drawing of the DGD dimer. The view direction is along the dimer 2-fold axis. One monomer is drawn with thin lines, the other one with thick lines. Every 50th residue in one subunit is labeled. The PLP cofactors are drawn in bold. Large and small filled spheres represent the ions bound at sites 1 and 2, respectively.

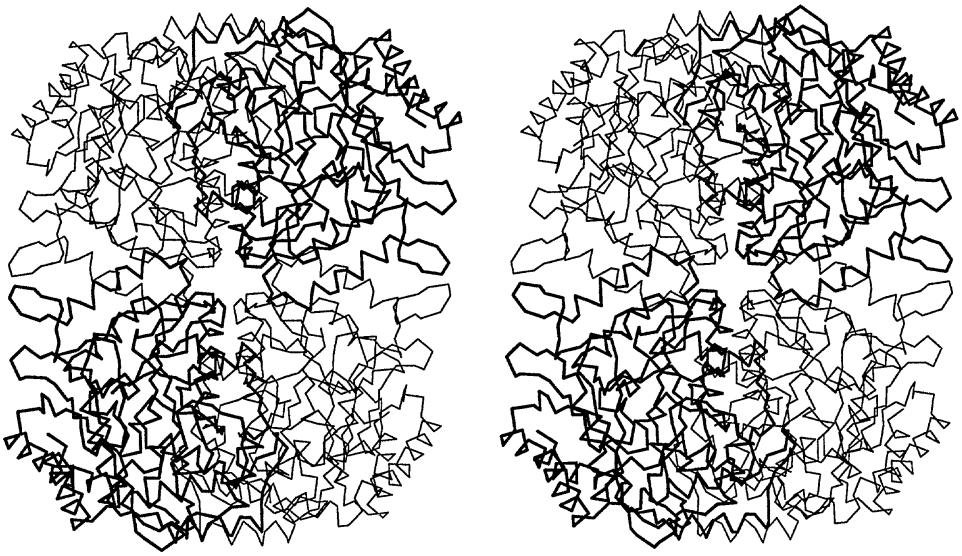

Figure 7. α-Carbon stereo drawing of the DGD tetramer viewed along one of the 3 2-fold axes of the tetramer. The axis relating the 2 dimers is horizontal and in the plane of the paper. The axis relating the 2 monomers of the dimer is vertical and in the plane of the paper. Two subunits are drawn with bold lines.

Crystal packing

The overall dimensions of the DGD tetramer are ~100 Å × 85 Å × 60 Å. The tetramer has crystallographic 222 symmetry, with the 2-fold axes intersecting at $(\frac{1}{2}, \frac{1}{2}, \frac{1}{6})$ and symmetry-related positions. As shown in Figure 8, the 6_4 screw axis generates a left-handed helix of tetramers along the *c* axis, with a large (diameter ~60 Å), solvent-filled channel at its center. This arrangement results in two types of packing contacts. The first, weaker contact (contact 1) involves only two C termini. Apart from a salt bridge between the C-terminal carboxyl group and Lys381, there are no specific protein-protein interactions. Furthermore, no ordered water molecules are found in the contact region. The second crystal lattice contact (contact 2) is made between helices 10 and 11 and their symmetry mates. Specifically, the regions around Gly325, where helices 10 and 11 are connected by a short turn, interact *via* a number of ordered water molecules. Interestingly, no direct protein-protein contacts are found. The C terminus of helix 3 and the following turn, where the structural sodium ion is found in both native structures (site 2), pack against helix 11. This partly covers the solvent exposed side of the metal binding site with the side-chain of Val332.

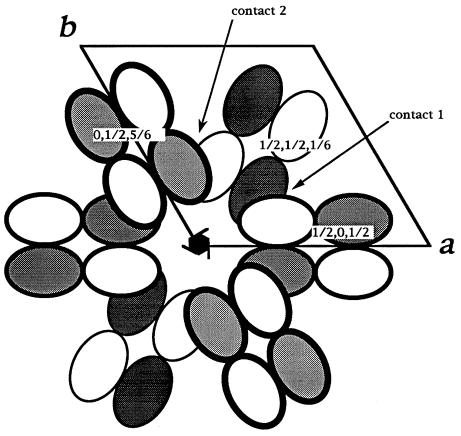

Figure 8. Schematic drawing illustrating the packing of the DGD tetramers in the crystal of space group $P6_422$. The 222 symmetry of the tetramers is crystallographic. The coordinates of the intersection points of 2-fold axes at the centers of the tetramers are indicated. The 6_4 screw axis at the origin produces a helix of tetramers with a hole of diameter 60 Å in the center. The 2 crystallographically distinct packing contacts (contacts 1 and 2) are described in the text.

Metal ion binding sites

In DGD-K^+, a potassium ion is bound at site 1 (Figure 9(a)), which is located close to the PLP phosphate group at the dimer interface. It is formed by two loop segments separated by ~220 residues in the sequence. The coordination geometry is octahedral with an average metal to ligand distance of 2.73 (±0.14) Å (see Table 2 for metal to ligand distances). The potassium ion is liganded by one carboxylate oxygen atom from Asp307, the main-chain carbonyl oxygen atoms of Leu78, Thr303 and Val305, the hydroxyl oxygen atom of Ser80, and a water molecule. The carboxylate group of Asp307 makes charge-moderating hydrogen bonds (and possibly salt bridges) with ND1 of both His77 and His304. The shortest K^+-ligand bond is formed with Asp307 OD1, as might be expected based on electrostatic considerations. The Asp-K^+ interaction is best

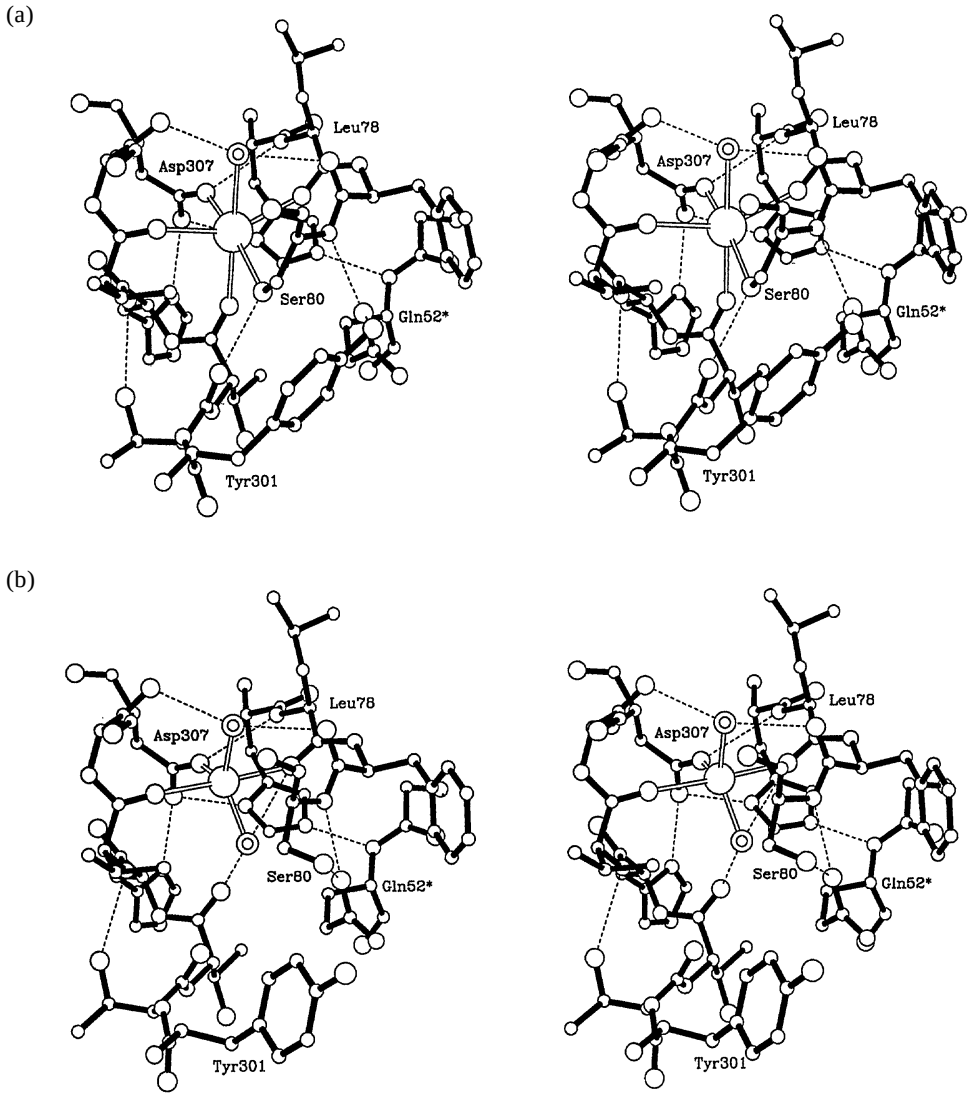

Figure 9. Stereo drawing of metal binding site 1 in DGD with (a) K^+ bound (DGD-K^+) and (b) Na^+ bound (DGD-Na^+). The metal ions are represented by large open spheres, water molecules by double spheres. Broken lines indicate hydrogen bonds. All ligands to both metal ions are oxygen atoms. K^+ is 6-coordinate with octahedral geometry and an average metal to ligand distance of 2.73 ($\pm$0.14) Å. Na^+ is 5-coordinate with trigonal bipyramidal geometry and an average metal to ligand distance of 2.33 ($\pm$0.16) Å. Residues contributed by the 2nd subunit in the dimer are labeled with an asterisk (*).

described as ''side-on'' *syn* (Glusker, 1991). The water ligand to the K^+ donates hydrogen bonds to the carbonyl oxygen atoms of Ser306 (2.74 Å) and Phe79 (3.08 Å).

In DGD-Na^+, a sodium ion is bound at binding site 1 (Figure 9(b)). The coordination geometry is trigonal bipyramidal with an average metal to ligand distance of 2.33 ($\pm$0.16) Å (Table 1). As in DGD-K^+, the metal ion interacts with the carboxylate group of Asp307 and with the carbonyl oxygen atoms of residues 78 and 305. The water molecule coordinated to the metal ion in DGD-K^+ is observed as well. Notable structural changes are observed for the other liganding groups. The trigonal bipyramidal geometry is a result of the replacement of both the Thr303 carbonyl oxygen atom and the Ser80 hydroxyl oxygen atom with a second water molecule. This change in structure is brought about by the different metal ion position in DGD-Na^+, a segmental movement of residues 300 to 305, and the $\sim$120° rotation of the Ser80 side-chain away from the metal, towards the active site. Both water ligands to the sodium ion are involved in hydrogen-bonding networks with atoms contributed by the protein. Wat509 hydrogen bonds to the carbonyl oxygen atoms of Ser306 (2.96 Å) and Phe79 (3.05 Å), while Wat519 interacts with the carbonyl oxygen atom of Thr303 (2.80 Å) and Leu78 (3.10 Å). The structural consequences of the exchange of ions at site 1 are not confined to the immediate surroundings of the metal ion, but also affect the conformation of the active site residue Tyr301 and other more distal regions of the structure (see below).

At site 2 in both native structures, a sodium ion is bound at the C terminus of helix 3 in a tight type II reverse turn (Table 1) preceding strand *a* of the central

Table 2

Metal to ligand distances

Ligand	DGD-K^+	DGD-Na^+
	Site 1	
	Potassium	Sodium
Leu78 O	2.70	2.36
Ser80 OG	2.84	(5.92)†
Thr303 O	2.74	(4.04)
Val305 O	2.87	2.60
Asp307 OD1	2.47	2.27
Wat530 O	2.73	—
Wat509 O	—	2.23
Wat519 O	—	2.19
	Avg. = 2.73 ± 0.14	Avg. = 2.33 ± 0.16
	Site 2	
	Sodium	Sodium
Ala95 O	2.33	2.39
Thr98 OG1	2.65	2.56
Thr98 O	2.42	2.52
Pro99 O	2.10	2.44
Leu102 O	2.61	2.31
Wat573 O	2.20	—
Wat526 O	—	2.22
	Avg. = 2.39 ± 0.22	Avg. = 2.41 ± 0.13

† The distances given in parentheses are for reference only. These atoms are not ligands to the sodium ion at site l in the DGD-Na^+ structure.

β-sheet of the large domain (Figure 10). The sodium ion is coordinated in nearly perfectly octahedral geometry by the main-chain carbonyl oxygen atoms of Ala95, Thr98, Pro99 and Leu102 and the β-hydroxyl oxygen atom of Thr98. A water molecule on the solvent side of the binding site completes the coordination sphere. The average metal to ligand distances are 2.39 (±0.22) Å in DGD-K^+ and 2.41 (±0.12) Å in DGD-Na^+ (Table 2). The closest negatively charged amino acid side-chain is that of Asp103 at a distance of ~6 Å, which interacts with the sodium ion *via* three water molecules. Site 2 is located close to the region where the N-terminal helix and loop of the other subunit interacts with the large domain, which is where significant changes in the backbone structure occur, as a consequence of the structural changes at site 1 upon exchange of ions. Notably, His16* hydrogen bonds to the carbonyl oxygen atom of residue 103 and is in van der Waals contact with C^β of Ala95.

Active site structure

The following description of the active site structure is based on the catalytically active form of DGD, that with K^+ bound at alkali metal ion binding site 1. Figure 11 illustrates the detailed structure of the DGD-K^+ active site. PLP is bound in a distinct cleft. In the orientation of Figure 11, the active site is delimited as follows: at the bottom, by the N terminus of the phosphate-binding helix, and the C termini of strands *e* and *f*; at the top, by the C-terminal loop from the three-stranded β-sheet, and the loop connecting helices 2 and 3; on the right, by strands *D* and *E* of the small domain β-sheet and a turn comprising residues 214 to 217; on the left, by the extended chain comprising residues 297 to 303 provided by the second subunit in the dimer; and, in front, by the extended chain connecting strand *b* and helix 5.

The following description of the active site structure begins with the groups directly contacting the coenzyme, proceeding counterclockwise from N-1 around the PLP ring. This is followed by the

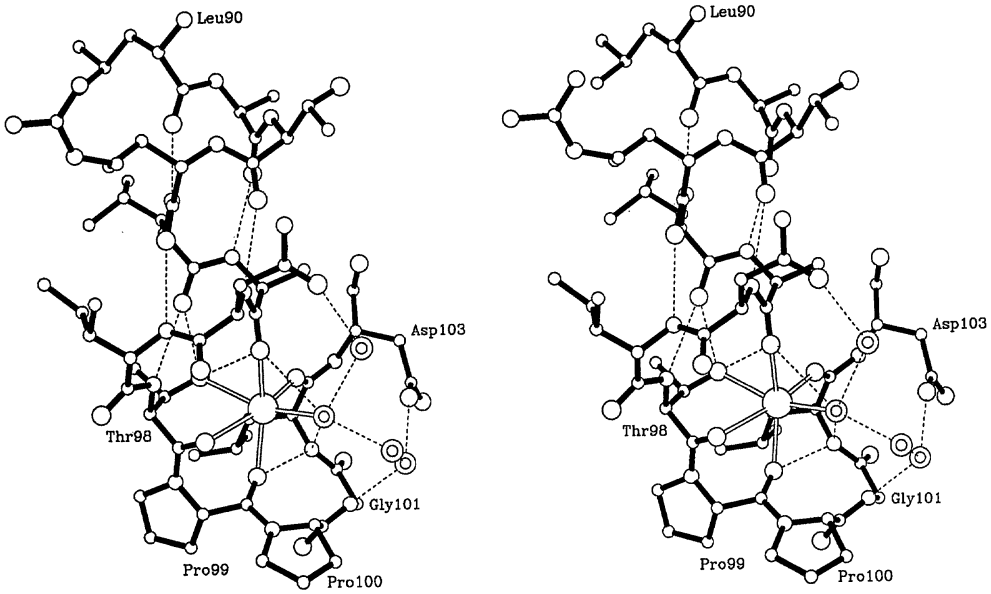

Figure 10. Stereo drawing of metal binding site 2 in DGD with Na^+ bound. The sodium ion is represented by the large open sphere and water molecules by double spheres. Broken lines indicate hydrogen bonds. All ligands to Na^+ are oxygen atoms. Na^+ is 6-coordinate with octahedral geometry and an average metal to ligand distance of 2.39 (±0.22) Å.

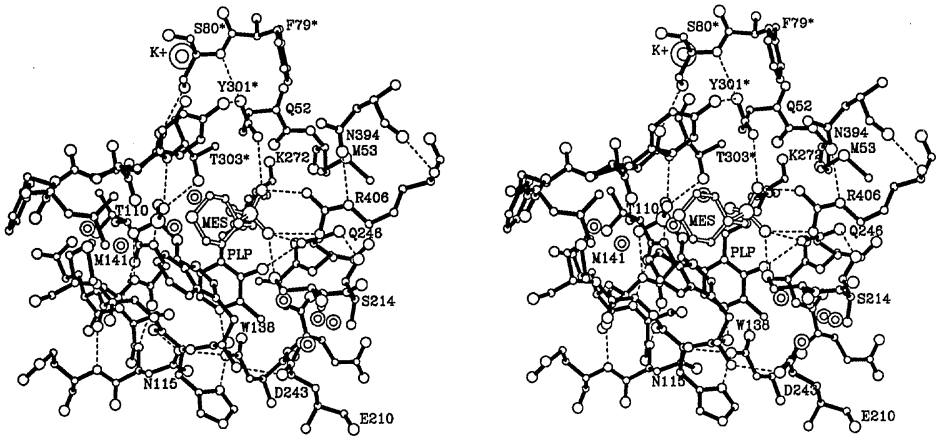

Figure 11. Stereo drawing of the DGD-K^+ active site. The bound Mes molecule is shown with open bonds. Broken lines indicate hydrogen bonds. Water molecules are represented by double spheres. The large double sphere at the upper left represents the K^+ ion bound to metal binding site 1. Residues contributed by the 2nd subunit in the dimer are labeled with an asterisk (*).

more distal features possibly relevant to the reaction mechanism.

The pyridine nitrogen atom (N-1) of PLP makes a strong hydrogen bond / salt bridge (2.73 Å) with the carboxylate OD2 from Asp243, and possibly interacts with OD1 (3.30 Å; see Table 3 for active site interatomic distances). Asp243 OD2 makes two hydrogen-bonding interactions, one with His139 and the other with the side-chain amide nitrogen atom of Asn113. These hydrogen bonds would impede any rotation of the Asp243 carboxylate group. The methyl group at C-2 is not involved in any specific interaction with the protein. The (presumably ionized) phenolic hydroxyl group at position 3 receives a hydrogen bond from the side-chain amide nitrogen atom of Gln246, and from the protonated aldimine nitrogen atom as well.

Table 3

Selected DGD-K^+ interatomic distances between potential hydrogen-bonding partners in the active site

Atom of residue 1		Atom of residue 2		Distance (Å)
Mes	OS1	Arg406	NH2	2.82
Mes	OS1	Gln52	NE2	2.87
Mes	OS2	PLP272	NZ	3.20
Mes	OS2	Wat550	O	3.32
Mes	OS3	Arg406	NH1	3.27
Mes	OS3	Ser215	OG	3.23
Mes	OS3	Gln246	NE2	2.77
Gln52	NE2	Tyr301*	OH	3.39
Gln52	NE2	Wat566	O	2.96
Gln52	OE1	Tyr301*	OH	3.00
Gln52	OE1	Ser80*	OG	3.30
Gln52	OE1	Ser80*	N	2.77
Gln246	NE2	PLP272	O3	2.81
Gln246	OE1	Ser214	OG	2.67
Asn394	OD1	Arg406	NE	3.17
Asp243	OD1	PLP272	N1	3.30
Asp243	OD2	PLP272	N1	2.73
Asp243	OD2	His139	ND1	2.65
Asp243	OD2	Asn115	ND2	2.88
Thr303*	N	PLP272	OP3	2.84
Thr303*	OG1	PLP272	OP3	2.79
Gly111	N	PLP272	OP1	3.15
Ala112	N	PLP272	OP2	3.13

At position 4, the original PLP aldehyde function has been transformed into an aldimine *via* reaction with the ϵ-amino group of Lys272. This is assigned as a protonated aldimine (Christen & Metzler, 1985) based on the strong absorbance of the crystals near 405 nm (E.H. & J.N.J., unpublished results). The positive charge on the nitrogen atom may be largely compensated by its interaction with PLP O-3' and OS2 from the Mes sulfonate group. The N-$C_{(4')}$-$C_{(4)}$-$C_{(3)}$ torsion angle has a value of $\sim 35°$ in both the DGD-K^+ and DGD-Na^+ models.

The phosphate ester at position 5 is involved in a total of nine hydrogen bonds, saturating the hydrogen-bonding capacity of its non-ester oxygen atoms. Gly111 and Ala112 lie at the N terminus of helix 4 and make hydrogen bonds *via* their amide nitrogen atoms to OP1 and OP2, respectively. The only other hydrogen bond donors to the phosphate group that originate from the protein are the amide and hydroxyl groups of Thr303*. Surprisingly, five well-ordered water molecules are hydrogen bond donors. There is no positively charged group as hydrogen bond donor that might directly compensate for the charge(s) on the phosphate group. The helix macrodipole (Hol, 1985) of helix 4 presumably partially fulfils this role. The $C_{(4)}$-$C_{(5)}$-$C_{(5')}$-OP4 torsion angle assumes energetically favorable angles of 64° in DGD-K^+ and 46° in DGD-Na^+, placing the ester oxygen atom on the back side (A face; Ford *et al*., 1980) of the coenzyme.

The PLP pyridine ring is sandwiched between Ala245 on the back and Trp138 on the front side (B face). The near perpendicularity of the Trp138 indole ring to that of PLP allows NE1 to interact with the

phosphate OP1 *via* a water molecule. One face of the Trp138 indole moiety makes a hydrophobic interaction with Met141, whereas the other contacts the morpholino moiety of the Mes buffer molecule found in the active sites of both native structures.

The Mes sulfonate group makes a strong double hydrogen-bonded ion pair with the guanidinium group of Arg406, which is contributed by the small domain. The side-chain amide oxygen atom of Gln394 is also within hydrogen bonding distance of the Arg406 guanidinium group. Ser215 donates an additional hydrogen bond to the sulfonate OS3. Located below Ser215 and hydrogen-bonding to the main-chain amide nitrogen atom of Trp138 is Glu210, whose carboxylate group interacts with four well-ordered water molecules.

The residues at the top of Figure 11 complete the active site structure. Metal binding site 1, where the largest differences between the DGD-K^+ and DGD-Na^+ structures are observed, is located in this region. The N-terminal segment contributes Gln52, which is part of a left-handed helical turn that reaches into the active site. The Gln52 side-chain amide group is involved in hydrogen-bonding interactions with the hydroxyl group of Tyr301*, a water molecule, and the main-chain amide nitrogen of Ser80*, whose β-hydroxyl group is a potassium ligand. The side-chain amide nitrogen atom of Gln52 donates a hydrogen bond to OS1 of the Mes sulfonate group. The aromatic rings of Tyr301* and Phe79* impart a hydrophobic character to this area.

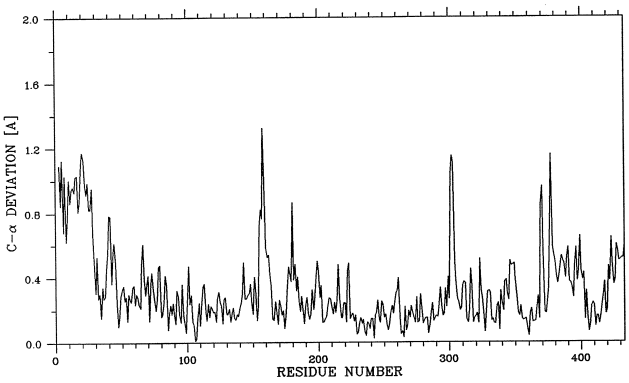

Figure 12. Distance between equivalent α-carbon atoms along the polypeptide chain for superimposed DGD-K^+ and DGD-Na^+ monomers. The 2 structures were superimposed by a least-squares fit using the 39 C^α atoms of the large central β-sheet in the PLP binding domain. The overall r.m.s. deviation, calculated with all 431 C^α atom pairs, is 0.32 Å. Note the large shift of the N terminus (residues 3 to 29).

Comparison of DGD-K^+ and DGD-Na^+

The *R*-factor of 17% observed between the DGD-K^+ and DGD-Na^+ data sets is largely due to a 1.2° rotation of the monomers with respect to each other in the dimer, i.e. a small change in quaternary structure. The r.m.s. distance between 431 equivalent C^α atoms is 0.32 Å when a least-squares superposition of the complete structures is made. Figure 12 presents a C^α-distance plot with the

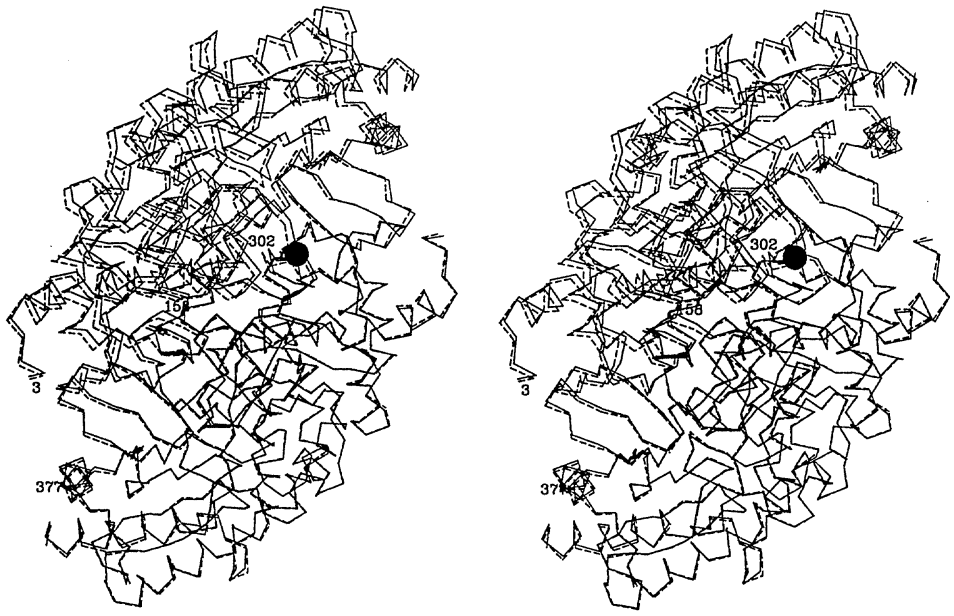

Figure 13. Stereo drawing showing a superposition of the DGD-K^+ (continuous lines) and the DGD-Na^+ (broken lines) dimer structure. The structures were superimposed using the 39 C^α atoms of the large β-sheet of the lower subunit in the Figure. The metal ion bound to site 1 of the lower subunit is represented by a filled sphere. Residues of the lower subunit with a difference in C^α positions > 1.0 Å (compare with Figure 12) are labeled. The change in quaternary structure upon metal exchange (1.2° rotation of the monomers with respect to each other) is evident from the difference in the positions of the upper subunits.

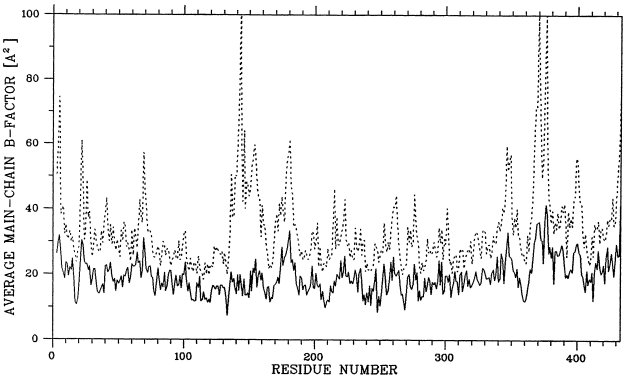

Figure 14. Distribution of main-chain *B*-factors in DGD-K^+ (continuous lines) and DGD-Na^+ (broken lines).

structures aligned using the large domains only. An overlay of the C^α traces of the two structures is shown in Figure 13. The N-terminal segment clearly makes the largest movement of any portion of the structure. The average displacement for residues 3 to 47 is 0.71 Å when the structures are aligned as above (0.91 Å for residues 3 to 29). The movement of the N-terminal segment is well modeled as that of a rigid body, with the DGD-K^+ structure assuming a slightly less ''open'' conformation. Several, more localized, structural differences between the two native structures are evident from Figure 12, with all peaks in the plot corresponding to loop regions. The loop comprising residues 155 to 159 takes part in both the dimer and the tetramer interface. Residues 301 to 303 are located in the active site and in metal binding site 1, and the shift in their C^α positions is easily accounted for by the different metal ions occupying site 1 in DGD-K^+ and DGD-Na^+. The smaller radius of the sodium ion leads to a shift in the positions at site 1 of residues 301 to 303 only. The main-chain conformation of residues 78 to 80 remains virtually unchanged. Finally, residues 369, 370, 376 and 377 are part of an irregular, disordered loop on the protein surface.

Figure 14 shows the distribution of the crystallographic *B*-factors over the DGD molecule for both native models. The correlation between the main-chain *B*-factors is good (linear correlation coefficient = 0.69), considering that different *B*-factor models were used in the refinement of DGD-K^+ and DGD-Na^+. The average *B*-factors for main-chain and side-chain atoms are, respectively, 19.4 and 22.1 $Å^2$ in DGD-K^+ and 32.8 and 35.8 $Å^2$ in DGD-Na^+. The higher *B*-factors in the DGD-Na^+ model are not a result of the merging of two data sets, since refinement against the synchrotron data alone yields very similar *B*-factors. A generally higher degree of disorder is observed in the DGD-Na^+ structure, with weak electron density for many side-chains of residues that are well ordered in DGD-K^+. In both native structures, high *B*-factors correspond to loops, while segments that are part of secondary structural elements generally have low *B*-factors, with the notable exception of helix 5 in DGD-Na^+.

Few side-chains adopt different conformations in DGD-K^+ and DGD-Na^+. Apart from some surface residues, several of which are disordered, there are only two residues with significantly different side-chain conformations, Ser80 and Tyr301 (Figure 15). As described above, the former residue is a ligand to the potassium ion in DGD-K^+ but not to the sodium ion in DGD-Na^+. This leads to a very different conformation of Ser80 (χ_1 is $-52°$ in DGD-K^+ and 64° in DGD-Na^+) and a significantly altered hydrogen-bonding network around metal binding site 1. Ser80 makes a hydrogen bond to Gln52* from the other subunit in DGD-Na^+. This forces Tyr301 to adopt a new conformation (rotation

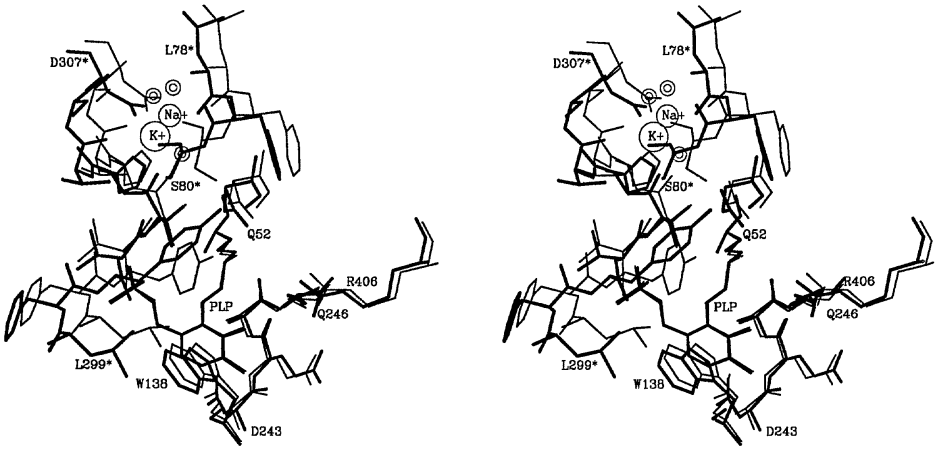

Figure 15. Stereo drawing showing a superposition of the local structures of DGD-K^+ (thick lines) and DGD-Na^+ (thin lines) around metal binding site 1. The atoms of the PLP cofactors were used for the superposition. Note that the residues shown in this Figure are contributed by both subunits in the dimer. Residues contributed by the 2nd subunit in the dimer are labeled with an asterisk (*). The quaternary structure change upon metal ion exchange at site 1 is reflected by the large change in structure in the upper half of the Figure. The side-chains of Ser80 and Tyr301 undergo large conformational changes.

about the Tyr301 C^{α}-C^{β} bond by ~90°), pointing away from Gln52*. Lacking a good hydrogen-bonding partner, the phenolic ring of Tyr301 is quite mobile in DGD-Na^+, as evidenced by its weak electron density.

More subtle changes involve the detailed structure of the dimer interface, and the structure of the phosphate binding site. Very weak electron density, suggesting substantial mobility, is observed for residues 142 and 143 in DGD-Na^+. These residues are located in the short helix 5 and interact with their symmetry mates in the dimer interface. Additionally, the structure of the water molecules hydrogen bonding to the PLP phosphate group is different, with one additional water molecule being observed in DGD-Na^+.

Comparison with aspartate aminotransferase

The X-ray structure of chicken mitochondrial aspartate aminotransferase (AAT) was the first of a classical, PLP-dependent enzyme to be solved (Ford *et al*., 1980). AAT is an α_2 dimer, as are many PLP-dependent enzymes, with its shape and dimensions being very similar to that of the DGD dimer. The domain structure and overall fold of AAT and DGD monomers show strong similarities, and the active site structures are moderately homologous, although there is no significant sequence identity (Keller *et al*., 1990; Pascarella *et al*., 1993).

An overlay of the C^{α} traces of the large domains of AAT and DGD is presented in Figure 16(a). Initially, the seven-stranded β-sheet and the phosphate-binding helix were used to perform a least-squares superposition of the two structures. This was followed by application of an overlap maximization algorithm (lsq_improve) implemented in the program O. This algorithm attempts to maximize the total number of overlapping C^{α} atoms (3. 8 Å overlap cutoff) that each belong to a contiguous string of three residues, while simultaneously maintaining a minimum in the r.m.s. difference in C^{α} positions. The resulting superposition has 140 homologous C^{α} atoms aligned (52% of the large domain) with a r.m.s. deviation of 2.1 Å. (158 C^{α} atoms can be aligned with a r.m.s. deviation of 2.7 Å using a 4.5 Å overlap cutoff.) As is evident from the Figure, all seven strands of the central pleated sheets correspond closely. Of the nine helices present in the DGD large domain, four (3, 4, 7 and 10) show substantial overlap with AAT within the 3.5 Å cutoff restriction. Of the remaining five helices, four (2, 6, 8 and 9) clearly have topologically equivalent partners in the AAT structure, although their sizes and orientations differ substantially.

A similar procedure was applied to the small domains, resulting in the overlay given in Figure 16(b). The three common helices are nearly completely conserved structurally. The largest differences are in the loop regions, which are generally larger in DGD. These enlarged loops, combined with the absence of the one-turn left-handed helix (near residue 352) in AAT, generate a four-stranded, antiparallel β-sheet in DGD that is not present in AAT.

The relative orientations of the large and small domains differ substantially between DGD and AAT. Figure 16(c) shows the complete monomers overlaid using the alignment for the large domains. The 10 Å displacement between the C termini exemplifies the difference in domain orientation, which can roughly be described as a counter-clockwise twist of the DGD small domain relative to the large one, in the view of Figure 16(c).

Figure 17(a) and (b) present the individual active site structures of DGD and AAT (Jansonius & Vincent, 1987), respectively, in analogous orientations. These structures were overlaid using a least-squares superposition of the PLP rings, of Asp243 with Asp222, and of Ala245 with Ala224 (where the first residues in this list are in DGD). Figure 17(c) shows the two structures together.

The most outstanding similarity in the active site structures is the nearly perfect conservation of the positions of the PLP pyridine nitrogen atom, the aspartate carboxylate group (from Asp243 in DGD) that is its hydrogen bond-salt bridge partner, and the imidazole nitrogen atom (from His139 in DGD) that hydrogen bonds to this carboxylate group. These interactions are known to be important to the mechanism of AAT (Yano *et al*., 1991, 1992). An addition to this trio is found in DGD, where the side-chain amide nitrogen atom of Asn115 donates a hydrogen bond to the aspartate carboxylate group. The methyl groups of the alanine residues (Ala245 in DGD) that abut the PLP rings also align well. The hydrogen bond from the phenolic hydroxyl group of Tyr225 to PLP O-3' in AAT, known to be mechanistically important (Goldberg *et al*., 1991), is replaced by one from the Gln246 side-chain amide nitrogen atom in DGD, with the difference in side-chain lengths being compensated by an adjustment in the main chain. A substrate α-carboxylate-binding arginine residue is found in both enzymes (Arg406 in DGD, Arg386 in AAT), although their positions differ. Arg406 is closer to PLP O-3' than is Arg386 in AAT in the open conformation.

Congruent with the variant mechanistic capabilities of the two enzymes, their active site structures show substantial differences. DGD-catalyzed decarboxylation may well involve Tyr301* and Gln52, which lie directly above the substrate binding site and have no counterparts in AAT (see Discussion). Both active sites have tryptophan located in front of the PLP ring, but the orientations of the indole ring planes differ substantially. In AAT, it is nearly parallel with the PLP ring plane, while in DGD it is almost perpendicular in the Mes-liganded structures. Lastly, Glu210 is found in DGD at the position corresponding to His189 in AAT.

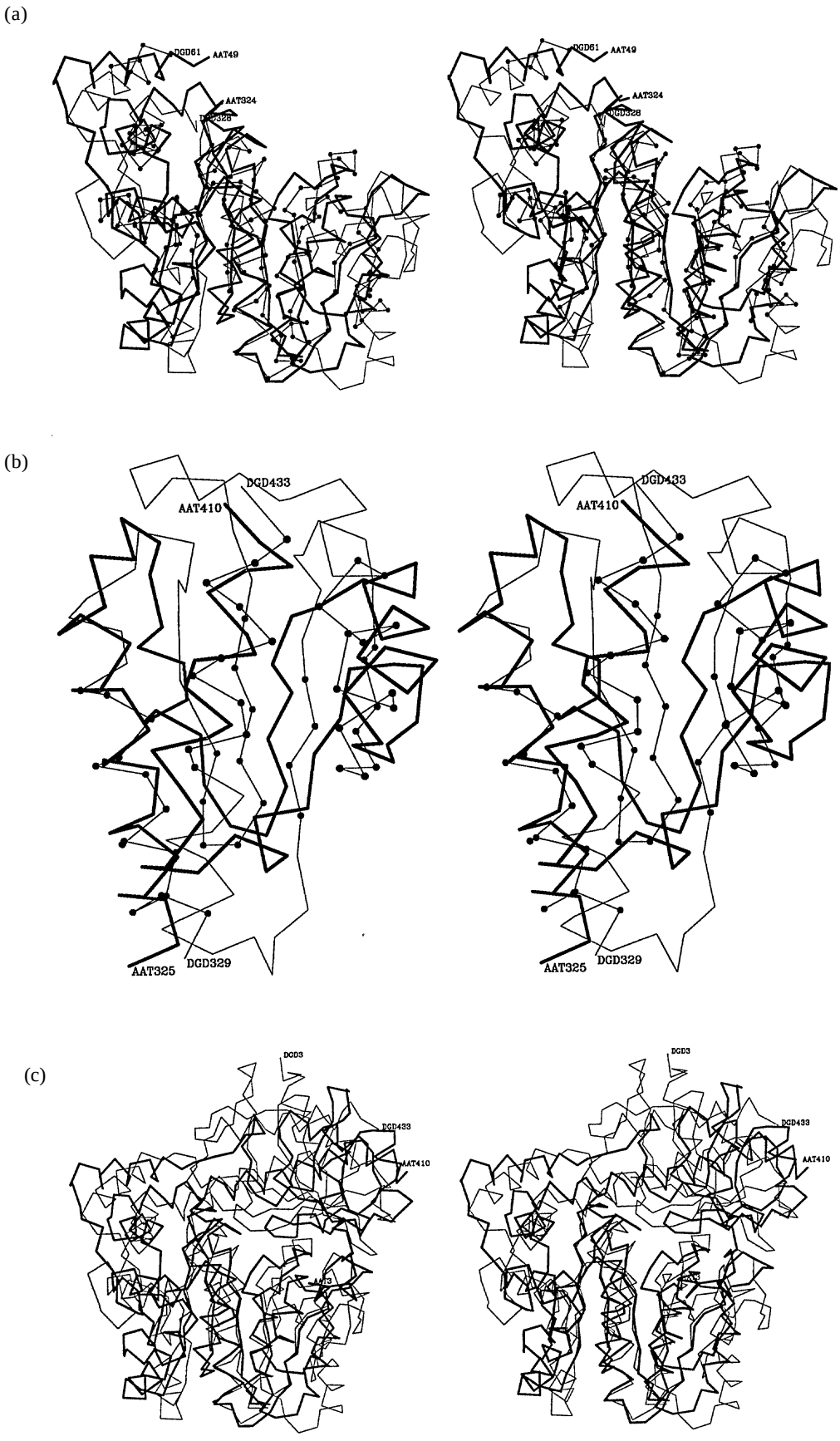

Figure 16. Stereo drawing showing a superposition of the structures of DGD (thin lines) and AAT (thick lines). Residues used in the least-squares fit are represented by filled circles. The first and last residue in each segment are labeled. (a) The large PLP binding domains. (b) The small domains. (c) The entire subunits superimposed based on the large domains as in (a).

External aldimine models

Hypothetical models of the L-isovaline and L-alanine external aldimine intermediates were built in order to rationalize structurally the mechanistic data available in the literature. The existence of these intermediates is dictated by the general mechanism of PLP catalysis. These models were

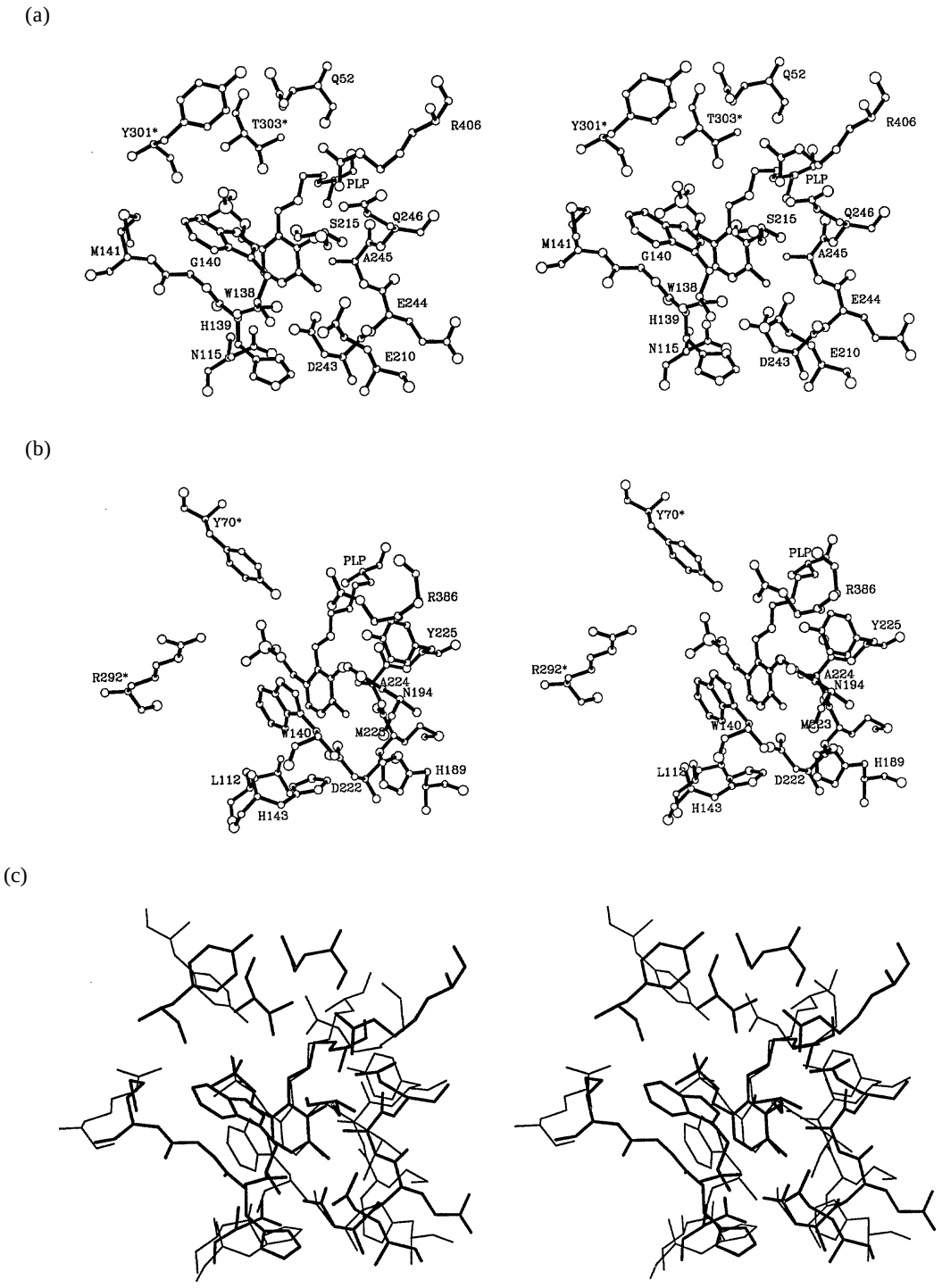

Figure 17. Stereo drawings comparing the active site structures of DGD and AAT. The views for (a), (b) and (c) are identical. Residues contributed by the 2nd subunit in the dimer are labeled with an asterisk (*). (a) DGD-K^+. The Mes buffer ion and bound water molecules are omitted. (b) AAT (holoenzyme, open conformation). (c) Superposition of DGD (thick lines) and AAT. The superposition was carried out using residues PLP, Asp243 and Ala245 in DGD and their spatial homologs PLP, Asp222 and Ala224 in AAT.

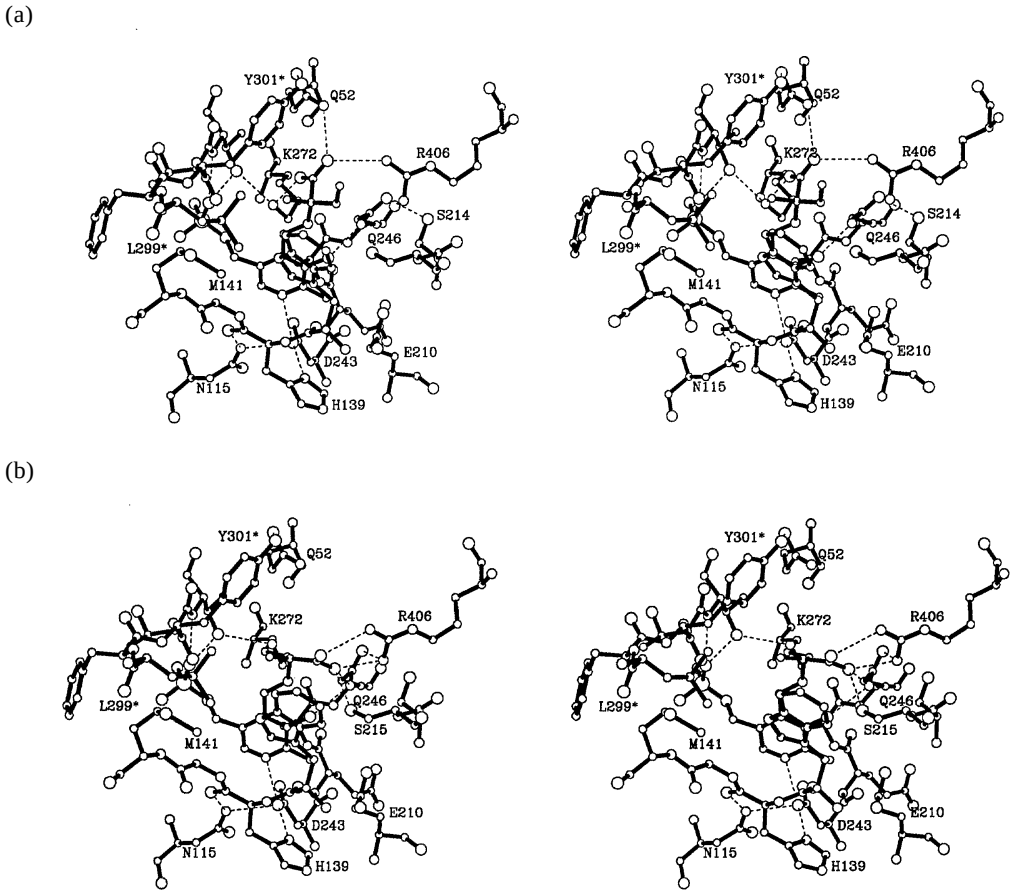

Figure 18. Stereo drawings of models for the L-isovaline and L-alanine external aldimine intermediates. The views for (a) and (b) are identical. Residues contributed by the 2nd subunit in the dimer are labeled with an asterisk (*). (a) L-Isovaline external aldimine model with the C^{α}-CO_2^- bond oriented perpendicular to the PLP ring plane, as would be expected for decarboxylation to occur. (b) L-Alanine external aldimine model with the C^{α}-H bond oriented perpendicular to the PLP ring plane, as would be expected for transamination to occur.

built with a minimal number of assumptions and protein manipulations.

The main assumption used in building the external aldimine models is that the scissile bond to C^{α} in this intermediate is perpendicular to the plane of the π-bonding system of the coenzyme. Dunathan (1966) proposed that PLP enzymes specifically orient the labile C^{α} bond in this manner as a mechanism to achieve reaction specificity. His argument is based on the observed stereoelectronic activation of carbon-hydrogen bonds in ketone enolization reactions in which the C-H bond perpendicular to the plane of the carbonyl group is preferentially labilized (Dunathan, 1966, and references therein).

The model of the L-isovaline external aldimine is shown in Figure 18(a). Adherence to Dunathan's proposal requires that the C^{α}-CO_2^- bond be oriented either as shown, or rotated by 180°. The latter possibility is ruled out by the presence of Trp138, and the lack of binding subsites for the alkyl substituents on the substrate when so oriented. One immediately notices that the orientation of the PLP ring has changed by a forward rotation in the view of Figure 11. The external aldimine is formed by a transimination reaction in which the substrate α-amino group replaces the ϵ-amino group of Lys258 in the aldimine linkage to PLP. In DGD, this results in steric clashes between the substrate carboxylate group and the protein, and the rotation of PLP is necessary in order to relieve these. The rotation is strictly analogous to that observed experimentally in AAT (Jansonius & Vincent, 1987), and was accomplished by changing only the $C_{(4)}$-$C_{(5)}$-$C_{(5')}$-OP4 torsion angle of PLP, from 64° to 91°. The forward rotation of PLP necessitates the reorientation of the Trp138 side-chain, as these are in van der Waals contact in the native structure.

The Lys272 side-chain is oriented so that it forms a hydrogen bond with the substrate carboxylate group. Likewise, the position of Arg406 is changed slightly to allow the guanidinium group to donate a single hydrogen bond to the substrate carboxylate group. The substrate carboxylate group accepts a third hydrogen bond from the side-chain amide nitrogen atom of Gln52. Finally, the side-chain of

Gln246 moves forward with PLP in order to maintain its hydrogen bond with O-3'.

The L-alanine external aldimine intermediate is shown in Figure 18(b). The model is similar to that for L-isovaline in that PLP, Trp138 and Gln246 are analogously reoriented. The different orientation about C^{α} is required by Dunathan's model, as L-alanine transamination proceeds *via* C^{α}-H bond cleavage. Arg406 moves to allow a double hydrogen-bonded salt bridge with the substrate carboxylate group. The hydroxyl group of Ser215 makes an additional hydrogen bond to the substrate carboxylate group, as does the side-chain amide nitrogen atom of Gln246.

The gross features of these external aldimine models such as the PLP and Trp138 reorientations have been confirmed by the structures of various inhibitors bound to DGD (V. N. Malashkevich & J.N.J., unpublished results).

Discussion

Active site location

The structure of the large domain of DGD is quite typical of open α/β folds (Brändén & Tooze, 1991). Brändén predicted that, in enzymes with this fold, ''the active site is at the carboxy edge of the β-sheet,'' and, in particular, that, ''functional residues are provided by the loop regions that connect the carboxy end of the β-strands with the amino end of the α-helices'' at ''topological switch points''. The latter are defined as places in the structure where the loops from the carboxy ends of adjacent β-strands follow paths to opposite sides of the central β-sheet. In DGD, there are two places where the structure completely fulfils this definition (between strands *c* and *b*, and strands *b* and *d*), yet these are not the location of the active site. Rather, in DGD, like in AAT, the active site is located at the carboxy ends of strands *e* and *f*. This is not strictly a topological switch point in that the loop from strand *f* goes directly into strand *g* rather than into the amino terminus of an α-helix. Nonetheless, the substrate-cofactor binding site largely satisfies the criteria of Brändén's prediction.

Alkali metal ion binding sites

DGD, with the alkali metal ion binding sites presented herein, is, to the best of the authors' knowledge, the second protein in which such sites have been observed crystallographically in a protein structure. Lijk *et al*. (1984) and Kooystra *et al*. (1988) described monovalent cation binding sites in the rhodanese structure. Non-specific binding of Na^+ and K^+ to proteins has been observed with subtilisin BPN' (Pantoliano *et al*., 1988), thermitase (Gros *et al*., 1991) and insulin (Gursky *et al*., 1992), but it appears that the alkali metal ions in these proteins do not have particular structural or functional roles. Rather, they bind to general cation sites, as has been clearly demonstrated for subtilisin BPN'. Crystallographic observation of the essential potassium ion in pyruvate kinase has remained elusive (Muirhead, 1987).

The novel nature of the alkali metal ion binding sites warrants particular scrutiny of the ion assignments. At least one potassium binding site was anticipated from the reported dependence of DGD activity and stability on potassium ions (Aaslestad *et al*., 1968). As McPhalen *et al*. (1991) have pointed out (p. 83), ''interatomic distances and angles are rarely restrained for ions during structure refinement, thus refined ion-ligand distances are good indicators of chemical identity for a protein-bound ion''. Such is the case with the DGD refinements: the distances and angles at the metal binding sites were fully unrestrained, and no electrostatic or van der Waals energy term was employed. Thus, the main criteria used for identifying the metal ions were: metal to ligand distances; comparison of metal *B*-factors with those of ligands; and difference electron density maps (Toney *et al*., 1993). Calcium was ruled out as a metal ion candidate for both DGD-K^+ and DGD-Na^+ by the low calcium content of the crystals (Toney *et al*., 1993).

The first site found was that near Pro99 (site 2). Initially, this was assigned as K^+ in both structures based on the literature data, but during refinement it became apparent that this assignment was incorrect. Refinement of a sodium ion with full occupancy at site 2 produced completely satisfactory results for both structures. The *B*-factors were in agreement with the values for the ligands, the average metal to ligand distance matched the standard value, and there was no significant difference electron density at the metal ion. The possibility that the observed density represented a tightly bound water molecule (which has the same number of electrons as Na^+) was also entertained, but the very close van der Waals contacts that would be made preclude this possibility.

The assignment of metals to site 1 in the two structures was made as follows. Initially, K^+ at full occupancy was refined in both structures. For DGD-K^+, the refinement with K^+ produced good results: the *B*-factor was 13 $Å^2$ for the ion compared with an average ligand value of 19 $Å^2$; the average metal to ligand distance matched the standard value for K^+; and difference electron density maps were featureless at the metal site. Refinement of Na^+, or Ca^{2+} at partial occupancies, against the DGD-K^+ data invariably resulted in very low metal ion *B*-factors and strong, positive difference electron density centered on the metal ion.

The refinement of K^+ at site 1 against the DGD-Na^+ data was unsatisfactory. Alternative models with partial occupancy for K^+ or Ca^{2+} produced *B*-factors above the average of the ligands and/or strong residual difference electron density centered on the metal. Also militating against the possibility of partial K^+ or Ca^{2+} occupancy is the fact that the electron density for the residues forming the binding site is clear and well defined. If the site were

partially occupied, with the shorter metal to ligand distances being due to an averaging of the distances of the occupied and unoccupied structures, then one would expect that the electron density for the residues forming the binding site would be diffuse compared with that in the DGD-K^+ structure. Refinement with Na^+ at full occupancy gave satisfactory results (Toney *et al*., 1993); the metal and ligand *B*-factors were compatible, and the observed average metal to ligand distance of 2.33 Å corroborates the Na^+ assignment, and weighs against the presence of Mg^{2+}.

Additional evidence suggests that the above assignments (DGD-K^+: K^+ at site 1 and Na^+ at site 2; DGD-Na^+: Na^+ at both sites) are correct. The buffers employed contained no added divalent metal ions, so that either Ca^{2+} or Mg^{2+} would have to be endogenous and/or very tightly bound. The Ca^{2+} content of the buffers was determined experimentally to be 10 to 30 μM (Toney *et al*., 1993), and Mg^{2+} is expected at a similarly low concentration. On the other hand, ~10 mM K^+ and 75 mM Na^+ were present in the DGD-K^+ buffer, and ~120 mM Na^+ was in the DGD-Na^+ buffer. It was previously demonstrated not only that K^+ is required for stability and activity, but that Na^+ and Li^+ are strongly inhibitory (Aaslestad *et al*., 1968). The location of site 1 near the active site, its acceptance of either K^+ or Na^+, and the structural rearrangements that accompany ion exchange suggest that this is the locus of inhibition.

Recent experimental results (Hohenester *et al*., 1994) provide possibly the strongest evidence that these are specifically alkali metal ion sites. Crystal soaking experiments with Li^+ clearly demonstrate Li^+ binding at site 1. Experiments with Rb^+ demonstrate the binding of this metal to both sites, although with low affinity to site 2. Similarly, Kooystra *et al*. (1988) used Cs^+ replacement with rhodanese to demonstrate two specific monovalent cation binding sites in this enzyme. Interestingly, the soaking experiments that produced the TlCl derivative of DGD did not give Tl^+ bound at site 1. This is presumably due to high selectivity at this metal binding site and the relatively low concentration (10 mM) of TlCl employed.

A cation binding site in rhodanese (Lijk *et al*., 1984; Kooystra *et al*., 1988) is similar to the structure of site 1 in DGD-K^+. This rhodanese site employs only oxygen ligands and has been shown to bind NH_4^+, Na^+ and Cs^+. The ligand geometry is distorted trigonal bipyramidal and a carboxylate oxygen atom is an equatorial ligand, in analogy with DGD site 1.

The structure of site 1 with K^+ bound is reasonably similar to those of several Ca^{2+} binding sites. All ligands are oxygen atoms, as preferred by the ''hard'' alkaline earth and earth metal ions. One difference is that Ca^{2+} sites are generally 7-coordinate, with one carboxylate group forming a bidentate interaction. Another is that Ca^{2+} sites, with the higher metal ion charge density, generally have more than one carboxylate group donating a ligand to the metal. Inhibition by divalent cations was reported by Aaslestad *et al*. (1968), and crystallographic experiments aimed at determining the structure of DGD bound to several of these are in progress.

At first glance, it is surprising that the exchange of Na^+ for K^+ at site 1 leads to a gross change in coordination geometry. Glusker (1991) presented data from the Cambridge Structural Database that show a clear preference for hexa- over pentacoordinate interactions by Na^+, and little preference between hexa-, hepta- and octacoordinate interactions (slightly favoring the latter) for K^+. The change in coordination number and geometry must be a consequence of restricted adaptability of the protein at the binding site. In order to maintain an octahedral coordination of Na^+, the protein structure would have to contract to accommodate the 0.3 to 0.4 Å average shortening of each of the metal to ligand distances. This would lead to steric clashes between the Ser80 side-chain and the carbonyl group of Thr302 unless substantial rearrangement of the polypeptide-chain around these residues were to occur. Instead, it is apparently easier for the protein to expand this part of site 1 and replace both the Ser80 and Thr303 interactions with a single one from a water molecule. The rearrangement of the Ser80 and Tyr301 side-chains that accompanies the exchange of ions likely accounts for the inhibitory effect of Na^+ and Li^+. This is further discussed below in conjunction with the catalytic mechanism.

Site 2 is one of the few known metal ion binding sites in a protein where there is a direct interaction between the metal ion and the C terminus of an α-helix. The paucity of such interactions is surprising given that the peptide carbonyl groups at the ends of helices are appropriate ligands for hard metals and that the helix macrodipole would provide electrostatic stabilization. By contrast, Hol (1985) found that approximately 60% of small, phosphate-containing molecules bound by proteins are bound at the N termini of α-helices. The lack of negatively charged ligands to the Na^+ suggests that the helix macrodipole may partially compensate the positive charge on the ion, although given the many examples of tight binding of alkali metal ions to neutral cryptands (Cram, 1986), this may be a moot point. Site 2 is located at the surface of the molecule (Figure 6), far from the active site. Combined with the high specificity for Na^+, this suggests that it serves a structural purpose only. The charge-dipole interaction surely stabilizes helix 3; this would be closely analogous to the experimentally demonstrated stabilizing effects of appropriately charged side-chain / helix dipole interactions in other proteins (Caffrey & Cusanovich, 1991; Nicholson *et al*., 1991; Eijsink *et al*., 1992).

Reaction specificity for various substrates

Previous solution studies on DGD provide an engaging set of experimental results to be correlated with the structural data. (1) α-Methyl-α-amino-

malonate is decarboxylated. (2) Transamination of α-keto acids produces only L-amino acids (Bailey & Dempsey, 1967; Bailey *et al*., 1970*a*). (3) Both D and L-alanine are decarboxylated, albeit with much smaller rate constants than for isovaline, but only L-alanine is transaminated (Bailey *et al*., 1970*b*). The ratio of decarboxylation rate constants for D and L-alanine is approximately 5:1. (4) The substrate specificity is not strict. L-Isovaline is decarboxylated only twice as fast as D-isovaline (Bailey & Dempsey, 1967). Increasing the side-chain length of α-keto acid substrates has, to a point, a moderate effect on the rate of transamination (Bailey & Dempsey, 1967). Keto acids with side-chains that are either large (e.g. phenylpyruvate) or charged (e.g α-ketoglutarate) are not utilized (Honma *et al*., 1972). (5) Decarboxylation of either isovaline or α-methylalanine does not proceed without amino group transfer to the coenzyme (Bailey & Dempsey, 1967; Aaslestad *et al*., 1968).

The external aldimine models shown in Figure 18 were built in order to aid in the structural interpretation of these data. As mentioned above, these models incorporate the proposal of Dunathan (1966) that the labile bond to C^{α} is perpendicular to the plane of the PLP ring in the aldimine intermediate. Orienting the labile bond in this way provides maximum σ-π orbital overlap in the transition state and thereby maximizes the reaction rate. The structure of the α-methylaspartate external aldimine intermediate in AAT (Jansonius & Vincent, 1987), in which the C^{α}-CH_3 bond (structurally analogous to the labile C^{α}-H bond of aspartate) is indeed perpendicular to the PLP ring plane, provides direct experimental support that this mechanism for PLP-dependent enzyme reaction specificity is employed.

In our model, decarboxylation of L-isovaline proceeds with the substrate carboxylate group perpendicular to the PLP ring plane, with the methyl group pointed towards Tyr301* and Met141, and with the ethyl group lying against the Trp138 indole ring. L-Alanine transamination proceeds with the labile C^{α}-H bond perpendicular to the PLP ring plane and on the same side as Lys272, with the carboxylate group interacting with Arg406, and with the methyl group placed as for L-isovaline. As mentioned above, the alternative orientations about C^{α}, differing by 180°, are ruled out by their steric incompatibility with the active site structure and the expected role of Lys272 as general base catalyst of the transamination reaction, by analogy to the AAT mechanism (Kirsch *et al*., 1984; Jansonius & Vincent, 1987; Toney & Kirsch, 1993).

These modeling results suggest that there are three distinct binding subsites in the DGD active site: A, B and C (Figure 19). Subsites A and B can both accommodate a carboxylate group. Subsite A appropriately orients the labile bond, maximizing stereoelectronic advantages and additionally providing the necessary general base catalysis for transamination (Lys272, see below). Subsite B may well be the favored carboxylate binding site, as it

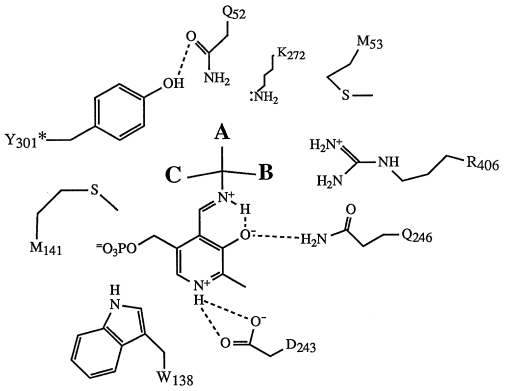

Figure 19. Schematic drawing illustrating the 3 proposed binding subsites in the DGD active site.

enables the double hydrogen bond / salt bridge with Arg406. Lastly, it is proposed that the shape and character of subsite C preclude carboxylate binding at this site, providing the key to the explanation of the results from solution studies.

The DGD-catalyzed decarboxylation of α-methyl-α-aminomalonate demonstrates that two carboxylate groups can be simultaneously and productively accommodated in the active site. This would occur in subsites A and B in the present model.

Transamination of α-keto acids to L-amino acid products would occur with the substrate α-carboxylate in subsite B, and proton transfer from the coenzyme C-4' to C^{α} would occur *via* subsite A, from the Lys272 side of the coenzyme-substrate adduct. This requires the α-keto acid side-chain to be located in subsite C. In order to yield D-amino acids from α-keto acids, DGD would have to bind the α-carboxylate group at subsite C. Figure 20 shows a solvent-accessible surface over the L-isovaline external aldimine model, which illustrates the proposed C subsite located between the PLP phosphate group and the Met141 side-chain. The introduction of a carboxylate group at this site would be unfavorable, as is apparent from the size, shape and proximity of the negatively charged PLP phosphate group, and lack of hydrogen bond donors. The inability of DGD to transaminate α-ketoglutarate provides corroborating evidence for this proposal that the α-keto acid side-chain binds in subsite C.

The results of the reaction specificity experiments with D and L-alanine are well explained by this model in which the C subsite cannot accept a carboxylate group. L-Alanine is transaminated with the hydrogen in the A, the carboxylate group in the B, and the methyl group in the C subsite, while it is decarboxylated with the carboxylate group in the A, the methyl group in the B, and the hydrogen in the C subsite, both orientations being acceptable. Decarboxylation of D-alanine would require the carboxylate group in the A, the hydrogen in the B, and the methyl group in the C subsite, which, again, is acceptable. Problems arise only when transamination of D-alanine is attempted. This requires the

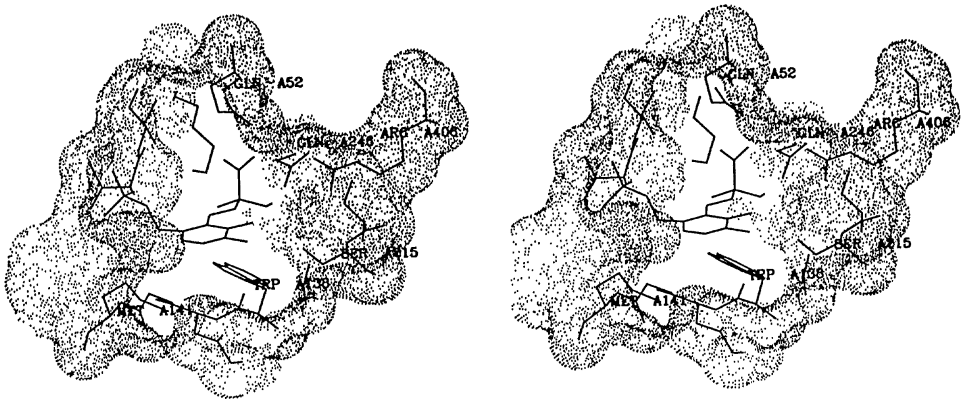

Figure 20. Solvent-accessible surface over the L-isovaline external aldimine model. The important feature of this surface is the large indentation that is seen between Met141 and the PLP phosphate group. This is the proposed binding subsite C. It is suggested that this pocket cannot accept a carboxylate group or a side-chain as large as a benzyl group, but that smaller side-chains are accommodated.

hydrogen in the A, the methyl group in the B and, unacceptably, the carboxylate group in the C subsite.

The weak discrimination between isovaline stereoisomers is explained by the ability of both subsites B and C to accept either a methyl or ethyl group. The C subsite is further probed by incrementally increasing the side-chain length of the α-keto acid substrates; the sevenfold preference of a methyl over a propyl side-chain, the fivefold preference of a propyl over an *i*-butyl side-chain, and the lack of reactivity of phenylpyruvate (Bailey & Dempsey, 1967) indicate the size of the pocket, which compares favorably with that seen in Figure 20.

The high selectivity of the transamination half-reaction (L-alanine transamination to decarboxylation rate constant ratio ~2000; Bailey *et al*., 1970*a*) likely stems, at least in part, from more favorable binding of the carboxylate group at the B *versus* the A subsite due to interactions with Arg406. For small dialkylglycine species, the likelihood of non-productive binding (i.e. with the carboxylate group bound at subsite B) appears significant. This would give observed decarboxylation rate constant values lower than the intrinsic ones (Fersht, 1985).

Catalytic mechanism

DGD presents a mechanistic challenge to the enzymologist. Its ability to catalyze rapidly both decarboxylation and transamination in its normal catalytic cycle is unusual. These two difficult, classical PLP-dependent reactions require very different chemical transformations (carbon-carbon bond scission *versus* 1,3-prototropic shift), yet, unlike most bifunctional enzymes that have two distinct active sites on separate domains, DGD catalyzes these reactions *via* a single active site. It is this intriguing mechanistic duplicity that we now attempt to explain on the basis of the active site structure.

Figure 21(a) presents a proposal for the mechanism of dialkylglycine decarboxylation catalyzed by DGD. The reaction sequence is initiated by the binding of the amino acid to the unliganded enzyme. Based on the similarity of the pK_a values observed in the V/K_{MeAla} pH profile and that determined by direct titration of the internal aldimine (J.W.K., unpublished results), the productive Michaelis complex is formed between the enzyme with an unprotonated aldimine nitrogen atom and the protonated amino acid substrate (or the kinetically equivalent pair, the protonated enzyme and the unprotonated substrate).

A major unresolved question is whether or not DGD undergoes a conformational change upon substrate binding, as does AAT, in which the small domain rotates by ~13° toward the large one, completely sequestering the substrate from solvent (McPhalen *et al*., 1992*a*). The active site of DGD is very open compared even with that of the open form of AAT. The Mes ligand in the present structures is not a substrate analog, and it may be that it binds tightly adventitiously without causing the conformational change that substrates might.

Transimination, yielding the external aldimine intermediate, follows Michaelis complex formation. This process occurs in three steps: proton transfer from the substrate amino group to the aldimine nitrogen atom (juxtaposing the highly reactive pair of protonated aldimine and primary amine), nucleophilic attack by the substrate on the protonated aldimine to give the *gem*-diamine and, finally, collapse of the *gem*-diamine to the external aldimine intermediate. The two available DGD structures are of the protonated internal aldimine enzyme, and in both of these the Lys272-PLP NE-$C_{(4')}$ bond is not coplanar with the PLP ring. This is similar to the structure of the protonated form of AAT (McPhalen *et al*., 1992*b*). The non-planar conformation of the aldimine linkage indicates that it is strained, and such strain would facilitate the formation of the gem-diamine intermediate from the Michaelis complex, since the geometry at C-4'

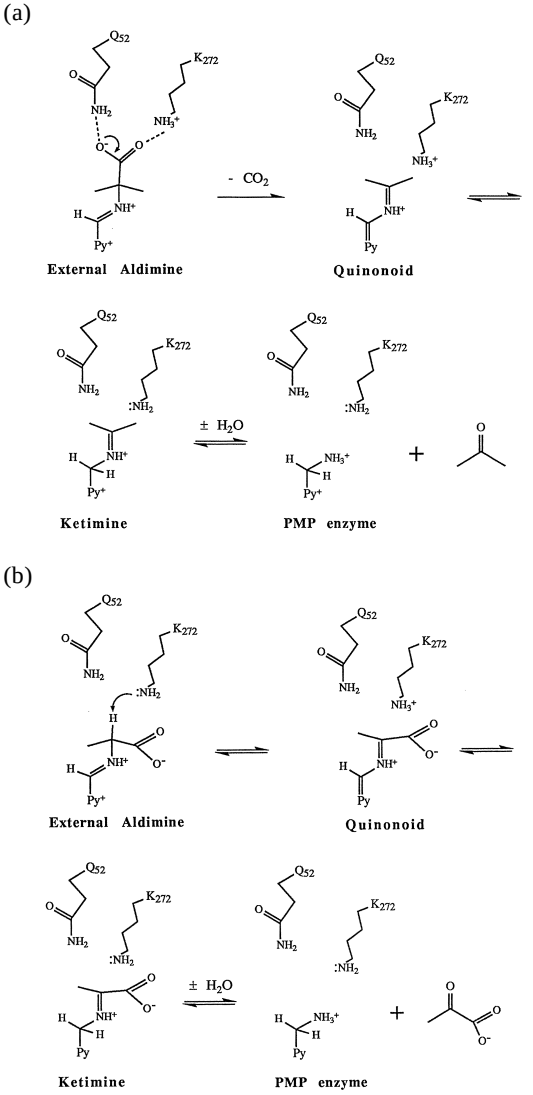

Figure 21. Proposed reaction mechanisms for the 2 half-reactions catalyzed by DGD. (a) Decarboxylation half-reaction. The hydrogen bonds to the substrate carboxylate group in the external aldimine intermediate are probably necessary in order to orient the C^{α}-CO_2^- bond perpendicular to the PLP ring plane, thereby stereochemically activating it. Loss of CO_2 gives the quinonoid intermediate, which is specifically reprotonated on C-4' of the coenzyme moiety to give the ketimine intermediate. The ketimine is then hydrolyzed to give the PMP enzyme form and the ketone product. (b) Transamination half-reaction. The C^{α}-H bond of the external aldimine intermediate is oriented perpendicular to the PLP ring plane and is probably deprotonated by Lys272 acting as a general base catalyst. Deprotonation of C^{α} gives the quinonoid intermediate, which can be reprotonated on C-4' of the coenzyme moiety to give the ketimine intermediate. Hydrolysis ensues, giving the PMP enzyme form and the α-keto acid product.

changes from trigonal to tetrahedral (sp^2 to sp^3) in this step.

A forward rotation of PLP by ~30° occurs concomitant with the formation of the external aldimine intermediate. Again, this necessitates that the Trp138 side-chain changes its conformation as well. This would occur before or synchronously with formation of the *gem*-diamine intermediate as even the small forward rotation of PLP in this step would likely cause an unacceptable steric clash. It may be that a conformational change of the Trp138 side-chain, such that it ''locks'' the substrate into the active site, largely takes the place of the domain closure type of substrate-induced conformational change such as occurs in AAT.

The next step is loss of CO_2 to give the quinonoid intermediate. Rates of decarboxylation reactions that proceed from an initial dipolar state to a charge neutralized one (as do PLP-dependent reactions) are known to be enhanced by non-polar media (Marlier & O'Leary, 1986, and references therein). Also, binding the carboxylate group of a dipolar decarboxylation substrate in a non-polar region of an antibody was recently shown to afford catalytic decarboxylation (Lewis *et al*., 1993; Ashley *et al*., 1993). Gallagher *et al*. (1989) suggested that electrostatic destabilization of the substrate carboxylate group in the reaction catalyzed by pyruvate-dependent histidine decarboxylase plays a major role in the decarboxylation step. It is thus surprising to find that the carboxylate group of the isovaline external aldimine is located in a hydrophilic binding pocket. The carboxylate group accepts three hydrogen bonds in our model: from Gln52, Arg406 and Lys272. These interactions, combined with the positive charge on Arg406 (and possibly Lys272), would selectively stabilize the ground state over the transition state, with a corresponding diminution of the decarboxylation rate. It is likely that a significant component of the enzymatic decarboxylation rate enhancement is the proposed stereoelectronic activation of the C^{α}-CO_2^- bond by maintaining it perpendicular to the PLP ring plane. Yet, in order to achieve the $\sim 10^9$-fold acceleration that DGD provides over the non-enzymatic rate (Kalyankar & Snell, 1962), this would require a much larger activation than has been observed in ketone enolization reactions (Corey & Sneen, 1956).

Hurley & Remington (1992) addressed a similar problem raised by the active site structure of isocitrate dehydrogenase, which catalyzes the decarboxylation of oxalosuccinate to α-ketoglutarate after the initial NAD^+-dependent dehydrogenation of isocitrate. These authors performed a set of electrostatic calculations that suggest that hydrogen bonding and electrostatic interactions between the protein and the labile carboxylate group, although they stabilize the ground state substantially, are catalytically advantageous. These interactions help drive the binding of the essential magnesium ion from the polarizable solvent into the non-polarizable active site where it provides greater stabilization of the unstable enolate intermediate. An analogy to DGD might be drawn where the interactions to the substrate carboxylate group, although stabilizing the ground state, enable the enzyme to populate the conformation of the external aldimine intermediate in which the C^{α}-CO_2^- bond is held perpendicular to

the PLP π-bonding system. Based on the structurally reasonable assumption that the external aldimine and carbanionic intermediates have no freedom of rotation about the C^{α}-N bond that would allow ''on-enzyme'' interconversion of conformers, only this conformation of the external aldimine leads to a C^{α} carbanion that can exploit the PLP electron sink (the catalytic potency of which is, compared with free PLP, enhanced by its various interactions with the protein), and enables transition state stabilization through σ-π orbital overlap. Clearly, the ground state stabilization provided by subsite A, although necessary, is more than offset by its transition state stabilization.

The canonical quinonoid intermediate is produced by C^{α}-CO_2^- bond scission and this delocalized carbanionic intermediate is most likely protonated by Lys272 to give the ketimine intermediate. Oddly, the quinonoid intermediate formed by dialkylglycine decarboxylation is not protonated at C^{α} of the substrate moiety (which would lead to an aldimine intermediate and non-oxidative decarboxylation as catalyzed by classical decarboxylases), rather it is invariably protonated at C-4' of PLP to yield the ketimine intermediate. Conversely, the quinonoid intermediate in the transamination half-reaction is protonated at C^{α}, most likely by Lys272 (by analogy to AAT). The reason for this differential quinonoid protonation in the decarboxylation *versus* the transamination half-reaction is not evident from the DGD structure. It is possible, for example, that the nascent CO_2 does not rapidly leave the active site and sterically prevents protonation of C^{α}, or that the substrate carboxylate group in the transamination half-reaction quinonoid makes interactions with the protein that allows a conformation appropriate for C^{α} protonation.

Hydrolysis of the ketimine intermediate completes the decarboxylation half-reaction and is likely a rapid process, general base catalyzed by Lys272. Kirsch *et al*. (1984) proposed a mechanism for ketimine hydrolysis in AAT that appears largely applicable to DGD.

The catalytic cycle is completed by a classical transamination reaction between the PMP enzyme and an α-keto acid substrate. Figure 21(b) outlines a mechanism for the transamination half-reaction. Bailey & Dempsey (1967) presented data that show a greater sensitivity of the overall reaction rate to the size of the α-keto acid substrate when L-alanine as compared with isovaline is used as the amino group donor; the overall reaction of α-keto acids with L-alanine comprises two transamination half-reactions, whereas that with isovaline comprises decarboxylation and transamination half-reactions. This result indicates that transamination of L-alanine is faster than decarboxylation of isovaline (i.e. that the decarboxylation half-reaction is largely rate-determining in the ping-pong kinetic mechanism).

Transamination between the PLP enzyme and an amino acid substrate such as L-alanine is initiated by the formation of the external aldimine intermediate, which would occur as outlined above for dialkylglycine species. The presence of a C^{α}-H bond (placed in subsite A) differentiates the L-alanine external aldimine intermediate from that of dialkylglycine species. The solution transamination of alanine by 3-hydroxypyridine-4-aldehyde, a model reaction for PLP-catalyzed transamination, is general base catalyzed (Auld & Bruice, 1967), as is the transamination reaction catalyzed by AAT. Lys258 is the sole general base catalyst in the AAT-catalyzed 1,3-prototropic shift (Toney & Kirsch, 1989, 1993), and the similar disposition of Lys272 in DGD compared with that of Lys258 in AAT (Figure 17) suggests that Lys272 fulfils an equivalent mechanistic role. The report of tritium transfer from C^{α} of L-alanine to C-4' of PLP in a brief abstract (Bailey *et al*., 1970*b*) would corroborate a single base mechanism, but these data must be interpreted with caution since the details of the experimental protocol are not available.

The 1,3-prototropic shift interconverting the external aldimine and ketimine intermediates could occur *via* either a concerted mechanism in which the quinonoid intermediate is avoided by simultaneous C^{α} deprotonation and C-4' protonation or a stepwise mechanism with a distinct quinonoid intermediate (Julin & Kirsch, 1989). No data pertaining to this question are available in the literature. Hydrolysis of the ketimine intermediate and release of the α-keto acid product complete the transamination half-reaction.

It appears, based on the above discussion, that the ability of DGD to catalyze both carbon-carbon bond scission (decarboxylation) and 1,3-prototropic shifts (transamination) resides in the compatibility of the mechanistic requirements of these two reactions, and the dual nature of the A and B binding subsites. Decarboxylation apparently requires only a carboxylate binding site that maintains the C^{α}-CO_2^- bond perpendicular to the PLP ring plane; transamination requires the C^{α}-H bond to be similarly oriented and, additionally, a general base catalyst, which is assigned as Lys272.

The change in conformation of Ser80 and Tyr301 upon exchange of K^+ for Na^+ provides the simplest explanation for the inhibition of DGD by Na^+ and Li^+. These residues are at the top of the substrate binding site, and the large rotation of the Tyr301 side-chain may disrupt the (productive) binding of substrate. It is not known whether the decarboxylation, transamination, or both of the half-reactions are inhibited by Na^+ and Li^+.

Comparison with other PLP-dependent enzyme structures

The structures of four other PLP-dependent enzymes (not counting glycogen phosphorylase, which utilizes PLP non-canonically) have been published. These include aspartate aminotransferase (Ford *et al*., 1980; Jansonius & Vincent, 1987), ω-amino acid aminotransferase (APT; Watanabe *et al*., 1989), tyrosine phenol-lysase (TPL; Antson

et al., 1993), and the β subunit of tryptophan synthetase (TS; Hyde *et al*., 1988). We now consider the relationships between these structures and that of DGD.

Chicken mitochondrial AAT was the first PLP-dependent enzyme to have its three-dimensional structure determined by X-ray crystallography (Ford *et al*., 1980). The folds of the AAT and DGD monomers are quite similar (Figure 16). The main differences are in the N-terminal regions, at the front of the active site at DGD helix 5, and in DGD helices 10 and 11, which form a single, long helix in AAT. The greatest difference in domain structure is in the relative orientations of the small and large domains.

The quaternary structure of DGD is tetrameric, unlike that of AAT, which is dimeric. The tetramer interface of DGD is formed by addition and extension of loops, the displacement of an α-helix, and a reorientation of the large subunits with respect to each other in the dimer provide the necessary interactions. In DGD, the small helix 5 and β-strand *c* (see Figures 4 and 5) are connected by a long loop that is involved in a number of interface interactions, while in AAT a longer helix is found in the spatially analogous position. Helix 6 makes several interface interactions, which is possible due to the greater length of the segments connecting helix 6 to β-strands *c* and *d* in DGD *versus* AAT. The larger connections allow this helix to move away from the central β-sheet. The long connection between β-strand *c* and helix 6 is particularly notable since it directly interacts with its symmetry mate in the tetramer interface. The small displacement of helix 6 from the β-sheet allows it to interact intimately with both its symmetry mate and the loop connecting helix 5 and strand *c*. Additionally, the large subunits in the DGD *versus* the AAT dimer are ''flattened out'' with respect to each other as evidenced by the greater angle between the phosphate binding helices in DGD (helix 4). This opens the DGD structure at the tetramer interface, facilitating dimer-dimer interactions.

The structural homology between the active sites of DGD and AAT (Figure 17) is mechanistically significant. An aldimine formed with an active site lysine residue has been found in every PLP-dependent enzyme to date. After the external aldimine intermediate is formed, this lysine residue is free to serve as a general acid / base catalyst. Stabilization of the common PLP intermediate, the quinonoid, involves delocalization of the electrons into the pyridine ring, which is most effective when the pyridine nitrogen atom is protonated. It is thus mechanistically satisfying to see the high degree of structural similarity between the residues in the DGD and AAT active sites (Asp243 *versus* Asp222, and His139 *versus* His143) that stabilize the protonated pyridine nitrogen atom. His139 in DGD and His143 in AAT are contributed by disparate secondary structural elements, highlighting their mechanistic importance. The conservation of a substrate α-carboxylate-binding arginine residue in DGD (Arg406; homologous to Arg386 in AAT) is apparently demanded by the need for DGD to transaminate pyruvate. Mehta *et al*. (1989, 1993) have shown that all aminotransferases utilizing α-amino acids conserve the three residues corresponding to DGD Lys272, Asp243 and Arg406, emphasizing the fundamental importance of these residues to the transamination mechanism. Lastly, PLP O-3' interacts with strong hydrogen bond donors in both DGD (Gln246) and AAT (Tyr225). The role in AAT for this interaction in maintaining unprotonated enzyme at physiological pH has been clearly demonstrated (Goldberg *et al*., 1991).

The structural differences between the DGD and AAT active sites are equally telling. Arg292 in AAT is largely responsible for the specificity of this enzyme for dicarboxylic substrates (Christen & Metzler, 1985; Jansonius & Vincent, 1987; Cronin & Kirsch, 1988), and its structural replacement by the hydrophobic residues Met141 and Trp138 in DGD is congruous with the specificity of DGD for alkane side-chains on its substrates. The singular presence in DGD of Gln52 and Tyr301 at the top of the substrate binding site likely explains the ability of DGD to decarboxylate amino acids.

The PLP phosphate binding sites in DGD and AAT are also different. Both lie at the N termini of structurally homologous α-helices, but the hydrogen bonding and charge interactions are not conserved. In both DGD-K^+ and DGD-Na^+, five water molecules are used as hydrogen bond donors, while the protein donates only four hydrogen bonds. In AAT, the protein donates all except one of the nine hydrogen bonds to the phosphate group (McPhalen *et al*., 1992*b*). Each enzyme saturates the hydrogen bonding capacity of the non-ester oxygen atoms, but AAT uses Arg266 as a hydrogen bond donor / salt bridging partner. These differences in phosphate liganding probably account for the much greater stability of PLP bound to AAT *versus* DGD (Toney & Kirsch, 1991; Bailey & Dempsey, 1967).

The fold of APT (Watanabe *et al*., 1989) is, despite low sequence identity (Yonaha *et al.*, 1992), closely homologous to that of DGD, and this enzyme is also tetrameric. The principal differences in structure are in the region of DGD helix 1, the loop between helix 5 and strand *c*, the loop between strand *c* and helix 6, and the relative orientations of the small and large domains. These differences produce a significantly smaller tetramer interface for APT.

The active site structure of APT, as presented briefly by Watanabe *et al*. (1991), is also similar to that of DGD. APT has residues corresponding to DGD residues Lys272, Asp 243, His139 and Glu210. Trp138 in DGD is replaced by tyrosine, whose side-chain is also nearly perpendicular to that of PLP. The similarity of the active site structures is consistent with the similarity of the chemistries catalyzed in the transamination half-reactions of these two enzymes.

Yonaha *et al.* (1992) present sequence alignments of APT with DGD and three other homologous PLP-dependent enzymes. This alignment combined with that between DGD and glutamate-1-semi-

aldehyde aminotransferase (Jäger, 1991) allows significant insight, in the light of the crystallographic results, into the structural relationships between these enzymes. The common feature of these enzymes is that they catalyze a half-reaction where the substrate α-carboxylate group is either non-existent or is not oriented (i.e. DGD) in the external aldimine intermediate such that it can interact with homologs of DGD Arg406. Importantly, in all the other enzymes examined the position corresponding to DGD residue 52 is not occupied by an amino acid capable of donating a hydrogen bond to the substrate. This coincides with the unique ability of DGD to catalyze decarboxylation, and provides corroborating evidence for the proposal that it is intimately involved in this reaction.

Of the enzymes examined, only APT shows significant homology at metal ion binding site 2. Thr98, Pro99, and Leu102 each donate ligands to the bound Na^+ and are conserved, suggesting that APT may also bind Na^+ at this site. Not surprisingly given their central mechanistic importance, residues corresponding to DGD Lys272 and Asp243 are conserved throughout this group. Another noteworthy conservation is that of DGD Glu210 and Pro211. Glu210 is located in the active site below Ser215 and in front of the PLP methyl group, in the view of Figure 11. Although the above discussion of the catalytic mechanism does not suggest a role for Glu210, its strict conservation throughout this diverse (i.e. low sequence homology) group of enzymes implies that it is significant either structurally or mechanistically. Its proximity to the reaction center suggests the latter. Finally, the sequence similarities in the region of the N-terminal β-sheet suggest that this structure is present in all of the enzymes.

Still other structural homologies between distantly related PLP-dependent enzymes have been detected. For example, Pascarella *et al*. (1993) have shown homology between serine hydroxymethyltransferase and both AAT and DGD. Antson *et al*. (1993) demonstrated that the fold of TPL is homologous to that of AAT and, by extension, DGD and APT. This combination of sequence and three-dimensional structural homology between mechanistically diverse enzymes raises the possibility that a large group of PLP-dependent enzymes have evolved from a common ancestral PLP binding protein, and that as these enzymes have adapted to new physiological roles they have essentially preserved the original fold of this ostensible ancestor. This is not an original suggestion (Alexander *et al*., 1994), but is strengthened by the present observations.

As noted above, Antson *et al*. (1993) presented the three-dimensional structure of TPL. Its fold is significantly homologous to that of DGD and it also is tetrameric. A remarkable distinction between the TPL and DGD structures is that the tetramer interface is formed from completely opposite sides of the constituent dimers. DGD forms the tetramer interface at the ''bottom'' of the dimer (i.e. symmetric interactions between helix 5 to strand *c* loops and helices 6) whereas TPL has a C-terminal extension that forms a large number of interface interactions at the ''top'' of the dimer. The functional unit of these enzymes is the dimer, and, given that no kinetic cooperativity has been observed, the advantage of tetramerization is not clear.

The structure of the PLP-dependent β subunit of TS was reported by Hyde *et al*. (1988). There is no significant structural homology between TS and DGD at the backbone fold or at the active site level.

Conclusions

The structure of DGD provides insight into the mechanisms by which proteins can specifically bind alkali metal ions, and how these metal ions can influence enzyme activity. This information may have significant implications for the study of the origins of specificity of transmembrane ion channels. A large number of enzymes are dependent on alkali metal ions for activity, and thus the structures of the DGD metal binding sites may only be the first of a large class of biologically important metal ion binding sites.

The substrate-reaction specificity and catalytic mechanism of DGD are explained by the presence of three distinct binding subsites proposed to occur in the active site. Subsite A orients the labile C^{α} bond perpendicular to the plane of the PLP ring, maximizing stereoelectronic advantages and additionally providing general base catalysis. Subsite B accepts the substrate α-carboxylate group in the transamination half-reaction, while subsite C cannot accept a carboxylate group. This latter restriction explains the available data on the reaction specificity for various substrates of DGD. The proposed catalytic mechanism for the decarboxylation half-reaction invokes stereoelectronic activation of the substrate α-carboxylate group bound at subsite A. The transamination half-reaction is likely general base catalyzed by Lys272, by analogy to the mechanism of AAT.

Lastly, the fold of DGD is homologous to those of AAT, APT and TPL, three PLP-dependent enzymes with little sequence homology, providing support for the proposal that this common fold is a general template for a large class of PLP-dependent enzymes.

Experimental Procedures

General

Crystals of DGD in space group $P6_422$ (hexagonal rods, typically 1.0 mm × 0.5 mm × 0.5 mm in size; $a = b =$ 152.7 Å, $c = 86.6$ Å; $\alpha = \beta = 90°$, $\gamma = 120°$) were obtained as described (Toney *et al*., 1991). Mes was obtained from Fluka, while sodium pyruvate and polyethyleneglycol 4000 were from Merck.

The CCP4 suite of programs (SERC, Daresbury, U.K.)

Table 4

X-ray diffraction data collection statistics

Data set	Resolution range (Å)	Number of reflections: Observed	Number of reflections: Unique	R_{merge} (%)†	Completeness (%)
(1) DGD-K^+	15–2.6	103,775	16,640	6.5	88
(2) DGD-Na^+	15–2.1	152,578	32,665	7.8	93
(3) $TlCl_3$	15–3.1	17,174	5634	7.7	50
(4) PPL-Cys-Hg	15–2.9	56,740	12,656	8.4	94
(5) EMTS	15–3.2	25,663	7519	7.5	74
(6) $KAuCN_2$	15–3.1	25,728	8119	8.1	72
(7) TlCl	15–2.7	77,022	15,745	8.3	92

All data, except DGD-Na^+ (image plate detector), were collected at ambient temperatures with 1 crystal per data set using a FAST area detector diffractometer. They were processed using the MADNES software package. The stabilization buffer for all crystals except DGD-K^+ was: 20% polyethyleneglycol 4000, 30 mM Mes-NaOH (pH 6.1), 100 mM sodium pyruvate, 20 μM PLP, 0.02% (w / v) sodium azide. The DGD-K^+ data set was collected from a crystal taken directly from the crystallization drop, under the conditions described previously (Toney *et al*., 1991).

† $R_{merge} = \Sigma|I - \langle I \rangle| / \Sigma I$.

was used for general crystallographic calculations. Version 5.7 of the program O (Jones *et al*., 1991) was used throughout for model building, and XPLOR version 2.1 (Brünger, 1990) was used for molecular dynamics refinement. Version 4.1 of the least-squares refinement package TNT (Tronrud *et al*., 1987) was employed in the later stages of refinement.

N-(5'-Phosphopyridoxyl)-L-cysteine was synthesized according to the general procedure described by Severin *et al*. (1969). This compound was reacted with 1.5 equivalents of methylmercuric chloride at room temperature for 30 minutes with shaking to produce *N*-(5'-phosphopyridoxyl)-*S*-methylmercuri-L-cysteine. The excess methylmercuric chloride was destroyed with β-mercaptoethanol and the product was isolated by chromatography (Severin *et al*., 1969). The free thiol contents before and after mercuriation were checked with Ellman's reagent (5,5'-dithiobis(2-nitrobenzoic acid)).

DGD apoenzyme was prepared by reacting PLP enzyme with excess 2-methylalanine and dialyzing the resulting PMP enzyme against several changes of 2 mM potassium phosphate, 2 mM Tris-HCl (pH 7.5) at 4°C.

X-ray data collection and reduction

Crystals were mounted in thin-walled glass capillaries with mother liquor at one end to prevent the crystal from drying out, and sealed with bee's wax. The long axis of the crystal, corresponding to the crystallographic *c*-axis, was oriented along the length of the capillary. All data (except the high-resolution DGD-Na^+ data) were collected at ambient temperatures using an Enraf-Nonius FAST area-detector diffractometer with a rotating anode generator operating at 40 kV and 50 mA. Reflections were measured in 0.15° frames, generally with exposures of 120 seconds.

The collection and initial processing of the FAST data were performed with the MADNES (Messerschmidt & Pflugrath, 1987) software, and the program PROCOR (Kabsch, 1988) was used to generate the raw intensity data. The data were then scaled and merged with the CCP4 programs ROTAVATA and AGROVATA. Structure factor amplitudes were calculated from the merged intensities using the CCP4 program TRUNCATE.

Two distinct native data sets were collected. The DGD-K^+ data were obtained from a crystal taken directly from the crystallization drop, which was formed by mixing 30 mg / ml DGD in 5 mM potassium phosphate buffer (pH 7.5), 15 μM PLP, and 0.02% (w / v) sodium azide with an equal volume of 15% (w / v) polyethyleneglycol 4000 in 15 mM Mes (neutralized with potassium hydroxide to pH 6.1), 100 mM sodium pyruvate, 15 μM PLP, and 0.02% (w / v) sodium azide (see Toney *et al*., 1991). The DGD-Na^+ data were from a crystal soaked in the same stabilization buffer (Table 4) used in the heavy-atom derivative soaks. The small difference in buffer conditions produces data sets that display a monotonically increasing *R*-factor with an average value of 17.4% between 10 and 2.8 Å resolution. By comparison, *R*-factors of ∼4% that were independent of resolution were obtained for distinct DGD-K^+ (and DGD-Na^+) data sets obtained from different crystals.

The DGD-Na^+ data are a combination of FAST data from15 to 3.6 Å and synchrotron data (EMBL, Hamburg) from 15 to 2.1 Å, collected on an image plate at 4°C. The image plate data were processed with the program MOSFLM (Leslie *et al*., 1986) adapted for image plates, then scaled, merged, and structure factor amplitudes calculated as for the FAST data. Almost 40% of the unique data to 3.6 Å resolution were rejected as ''overloads'' during the processing of the synchrotron data. Since a complete low-resolution synchrotron data set of DGD-Na^+ was not available, FAST data to medium resolution were used to complement the high-resolution synchrotron data. Statistics for the native and derivative X-ray data sets are presented in Table 4.

Heavy-atom derivatives and phase calculation

All heavy-atom derivatives were isomorphous with the DGD-Na^+ structure. It was not possible to solve the heavy-atom structures using the DGD-K^+ data, in spite of essentially identical cell constants for both native data sets.

Table 2 collects data on the preparation and analysis of the heavy-atom derivatives. The PPL-Cys-Hg derivative was prepared by reconstituting apoenzyme with an excess of *N*-(5'-phosphopyridoxyl)-*S*-methylmercuri-L-cysteine. The reconstituted enzyme was crystallized by macroseeding (Thaller *et al*., 1981) with native crystals. The aim was to produce a derivative with a single, fully occupied heavy-atom site near the coenzyme. As seen in Table 5, this was not the result. Based on the known substrate specificity

of DGD and the ease with which coenzyme is dissociated from it (Aaslestad *et al*., 1968), an explanation for the absence of any detectable mercury at the active site in this derivative is that the mercuriated compound is readily dissociated from the active site and subsequently reacts with two highly reactive cysteine residues. The demercuriated phosphopyridoxylcysteine is expected to bind more tightly to the active site than does PPL-Cys-Hg due to the smaller side-chain on the amino acid moiety.

The remaining derivatives were prepared by soaking native crystals in solutions containing the appropriate heavy-atom compound, under the conditions given in Table 5. The lengthy soaking times are not necessarily required to produce the derivatives, but resulted from unintended delays in data collection. Mercury-containing compounds are not well tolerated in general by the crystals; at concentrations exceeding 0.5 mM, most compounds crack the crystals within seconds. The two useful mercury derivatives were obtained with relatively unreactive compounds at very low concentrations.

The major sites for all derivatives were found with vector searches of difference Patterson maps using the CCP4 program VECSUM. These sites were refined against the centric data (CCP4 program REFINE; centric zones: 0*kl*, *h*0*l*, *hk*0 and *hhl*), ''best'' MIR phases were calculated (CCP4 program PHASE), and double difference Fouriers were used to locate minor heavy-atom sites. Final heavy-atom refinement produced the results given in Table 5. These heavy-atom structures were then used to calculate the final, ''best'' MIR phases. Figure of merit weighting in the electron density map calculation with the final phases yielded the MIR map. Inclusion of the available anomalous scattering phase information did not have a significant effect on the quality of the electron density map.

Solvent flattening

The initial 2.8 Å resolution DGD-Na^+ MIR map calculated in the space group $P6_222$ clearly showed the molecular boundary as well as some secondary structural elements. The presence of left-handed α-helices in the map allowed the assignment of the true space group, $P6_422$. The heavy-atom positions were adjusted accordingly and phases recalculated. The MIR map was not clear enough to begin confidently building the model. The calculated 61% (v / v) solvent content of the crystals suggested that solvent flattening (Wang, 1985) might prove useful. During this procedure, the reciprocal space averaging program of Leslie (1987) was used to calculate the molecular envelope.

Given that the accuracy of the molecular envelope is critical to the success of solvent flattening, the strategy used during the solvent flattening procedure was to begin at a solvent content that would avoid the danger of flattening protein portions of the map and to gradually increase it to just below the calculated value for the crystal, improving the molecular envelope with each increase in solvent content. For each solvent content value, the MIR phases and electron density map were initially used and the calculated phases from each flattening cycle (∼5 cycles per solvent content needed for convergence) were combined with those from the previous cycle. The starting value for the solvent content was chosen to be 25%. After flattening, the resulting map was used to calculate a molecular envelope at 35% solvent content. This new envelope was then employed in flattening the original MIR map. In this way, the solvent content used for flattening the MIR map was increased in four steps to 55%, with the intention that the first three steps would yield an optimal molecular envelope for the final solvent flattening procedure at 55% solvent content. The map so obtained was judged to have significantly better connectivity and structural detail than that from a single round of solvent flattening at 55% solvent content.

Model building and refinement

The DGD-Na^+ map flattened at 45% solvent content was used to calculate a set of ''bones'' (Jones & Thirup, 1986). These were manually rebuilt while consulting both the 45% and 55% solvent-flattened maps. From the rebuilt bones, 380 C^α coordinates (88% of the molecule) were obtained. The automatic, data base-oriented model building algorithms implemented in the program O were used to construct an initial model from the C^α coordinates and the published sequence (Keller *et al*., 1990).

The initial model was subjected to slow-cooling molecular dynamics refinement (Brünger *et al*., 1990) using XPLOR with data between 15 and 2.8 Å resolution. Phase restraints with phases from the 45% solvent flattening procedure were employed during this first refinement only. The crystallographic *R*-factor was reduced from the initial value of 52% to 31%.

Combination of calculated partial model and MIR phases, and σ_a-weighting (used throughout in map calculations employing phase combinations or partial model phases; Read, 1986), produced a map that was

Table 5

Heavy-atom derivative soaking conditions and refinement statistics

Compound	Concn. (mM)	Soak time (weeks)	Site and relative occupancy Cys258	Cys350	Cys60	Cy386	ΔF† (%)	$R_{centric}$‡ (%)	Phasing power (f_H / E)§
(1) $TlCl_3$	1	6	0.65	0.65	—	—	14.9	47	1.78
(2) PPL-Cys-Hg	0.030	12	0.63	0.73	—	—	15.8	51	1.71
(3) EMTS	0.020	6	0.99	1.00	0.46	—	19.3	40	2.21
(4) $KAuCN_2$	1	6	0.99	0.82	0.59	—	21.5	44	2.08
(5) TlCl	10	28	0.95	0.81	0.82	0.51	23.7	44	2.04

The derivative data were used in phase calculations to the resolution limits given in Table 4.

† $\Delta F = \Sigma|F_{der} - F_{nat}| / \Sigma F_{nat}$ with respect to DGD-Na^+, computed over the resolution ranges given in Table 4.

‡ $R_{centric} = \Sigma||F_{der} \pm F_{nat}| - F_H(calc)| / \Sigma|F_{der} - F_{nat}|$. These values were calculated for data between 15 Å and the respective high-resolution limits given in Table 4, with the exception of the TlCl data set, where $R_{centric}$ was calculated for data to 2.8 Å resolution. The centric zones are 0*kl*, *h*0*l*, *hk*0 and *hhl*.

§ The average computed over the resolution ranges given in Table 4. f_H = calculated r.m.s. heavy-atom structure factor amplitude, E = r.m.s. lack of closure error.

solvent flattened as above for the MIR map. This second solvent flattened map enabled two out-of-register corrections of one and two residues, and the addition of 50 residues. Main and side-chain adjustments were performed manually. Molecular dynamics refinement then reduced the *R*-factor from 33% to 26%.

A second phase combination of partial model and MIR phases produced a map that allowed a final, four residue out-of-register correction, and the completion of the structure. The model was again manually rebuilt. A final dynamics refinement employing this third DGD-Na^+ model reduced the *R*-factor from 30% to 21%.

The resulting DGD-Na^+ model was used directly as the initial model for molecular dynamics refinement against the DGD-K^+ data set (15 to 2.8 Å data only). No rigid body restrictions were employed. The initial *R*-factor of 31% was reduced to 23% using a standard slow-cooling protocol. The DGD-K^+ model so obtained showed small but significant changes compared with the DGD-Na^+ model (see Results).

Both the DGD-K^+ and DGD-Na^+ models obtained with XPLOR were manually adjusted according to difference maps and subsequently refined with TNT using 15 to 2.6 Å data for the DGD-K^+ model and 15 to 2.8 Å data for the DGD-Na^+ model.

Initially, water molecules were not included in the models. After 12 cycles of TNT refinement, large peaks in $(F_o - F_c)$, α_{calc} maps indicated some well-defined solvent molecules. The program SOLVENT (written by J. P. Priestle), which analyzes difference map peaks for hydrogen bonding potential and close contacts, was used to add water molecules in the form of oxygen atoms. Only peaks higher than 4σ in the $(F_o - F_c)$, α_{calc} maps were tested with SOLVENT.

Two further cycles of manual main and side-chain rebuilding, positional and grouped *B*-factor refinement, and addition of water with SOLVENT were performed. Only water molecules with *B*-factors below 65 $Å^2$ were retained. A total of 145 and 91 water molecules were introduced into the DGD-K^+ and Native B models, respectively, at this point. The *R*-factors for the models at this stage were 19.1% and 19.2% for DGD-K^+ and DGD-Na^+, respectively.

A strong, spherical peak near Pro99 in the $(F_o - F_c)$, α_{calc} maps for both DGD-K^+ and DGD-Na^+ was interpreted as a bound sodium ion (Toney *et al*., 1993).

The fit of the published sequence (Keller *et al*., 1990) to the density was unacceptable in two places at this stage: positions 81 to 83 and positions 308 to 313. Various model building attempts were unsuccessful in resolving the discrepancies. This prompted a resequencing of several G + C-rich regions of the dgdA gene. The original and revised sequences, which have been submitted to GenBank, are given below along with the nucleotide position and translation (Scheme 1). Amino-terminal sequencing of the recombinant protein showed the absence of an amino-terminal Met, and verified the identities of the next 38 amino acid residues (J. W. K. & M. O. Lively, unpublished results).

In addition, the protein used for crystallization contained two inadvertent mutations produced by tac polymerase, N15H (Toney *et al*., 1991) and G81E. The model was changed according to the sequence corrections,which brought the sequence and electron density data into agreement.

The two new models were refined with TNT using free individual *B*-factors for DGD-Na^+ and data from 8 to 2.1 Å resolution, while for DGD-K^+ restrained isotropic *B*-factors were refined and data from 8 to 2.6 Å were employed.

After refinement of the new models, DGD-Na^+ difference electron density maps showed strong positive density near Asp307, and a second sodium ion (Toney *et al*., 1993) was introduced. Spherical density surrounded by six oxygen ligands at the same position in the DGD-K^+ map allowed a potassium ion to be assigned to this site (Toney *et al*., 1993).

Further refinement with TNT combined with the introduction of more water molecules (total of 229) in the DGD-Na^+ model resulted in the final models (Table 6), which have been described. No attempt was made to refine

```
                    GlyGluMet
Original:    151    GGCGAGATG
Revised:     151    GGGCAGATG
                    GlyGlnMet

                    GlyIleValSer
Original:    241    GGAATCGTGTCG
Revised:     241    GGAATGCTGTCG
                    GlyMetLeuSer

                    SerAspArgCysProProAlaGlyVal
Original:    916    TCCGATCGCTGCCCCCCGGCGGGCGTC
Revised:     916    TCCGATCCGCTGCCC    GCGGCGGTC
                    SerAspProLeuPro    AlaAlaVal
```

Scheme 1

Table 6

Crystallographic refinement statistics

	DGD-K^+	DGD-Na^+
Resolution (Å)	8–2.6	8–2.1
Reflections†	16,057	32,089
R-factor (%)‡	17.6	17.8
Number of atoms in final models:		
Protein	3281	3048§
Solvent	145	229
Mes	12	12
Potassium	1	0
Sodium	1	2
Average *B*-factor ($Å^2$):		
Main-chain	19.4	32.8
Side-chain	22.2	35.8
Solvent	38.8	56.7
r.m.s. deviation from ideal:‖		
Bond lengths (Å)	0.013	0.011
Bond angles (deg.)	2.5	2.2
Trigonal planarity (Å)	0.005	0.004
Non-trigonal planarity (Å)	0.009	0.008

† No amplitude cut-off applied.

‡ *R*-factor = $\Sigma|F_{obs} - F_{calc}| / \Sigma F_{obs}$.

§ Atoms of disordered side-chains were refined with zero weight.

‖ The r.m.s. deviation values are those supplied by the TNT refinement package.

the occupancies of the DGD-Na^+ solvent molecules, resulting in artificially high temperature factors for the less populated ones.

References

Aaslestad, H. G. & Larson, A. D. (1964). Bacterial metabolism of 2-methylalanine. *J. Bacteriol.* **88**, 1296–1303.

Aaslestad, H. G., Bouis, P. J., Jr, Philips, A. T., Larson, A. D. (1968). Characterization of a decarboxylation-dependent transaminase. In *Pyridoxal Catalysis: Enzymes and Model Systems* (Snell, E. E., Braunstein, A. E., Severin, E. S. & Torchinsky, Y. M., eds), pp. 479–490, Wiley Interscience, New York.

Alexander, F. W., Sandmeier, E., Mehta, P. K. & Christen, P. (1994). Evolutionary relationships among pyridoxal-5'-phosphate-dependent enzymes. Regiospecific α, β and γ subgroups. *Eur. J. Biochem.* **219**, 953–960.

Antson, A. A., Demidkina, T. V., Gollnick, P., Dauter, Z., Von Tersch, R. L., Long, J., Berezhnoy, S. N., Phillips, R. S., Harutyunyan, E. H. & Wilson, K. S. (1993). Three-dimensional structure of tyrosine phenol-lyase. *Biochemistry,* **32**, 4195–4206.

Ashley, J. A., Lo, C.-H. L., McElhaney, G. P., Wirsching, P. & Janda, K. D. (1993). A catalytic antibody model for PLP-dependent decarboxylases. *J. Amer. Chem. Soc.* **115**, 2515–2516.

Auld, D. S. & Bruice, T. C. (1967). Catalytic reactions involving azomethines. IX. General base catalysis of the transamination of 3-hydroxypyridine-4-aldehyde by alanine. *J. Amer. Chem. Soc.* **89**, 2098–2108.

Bailey, G. B. & Dempsey, W. B. (1967). Purification and properties of an α-dialkyl amino acid transaminase. *Biochemistry* **6**, 1526–1533.

Bailey, G. B., Chotamangsa, O. & Vuttivej, K. (1970*a*). Control of pyridoxal phosphate enzyme reaction specificity studied with α-dialkylamino acid transaminase. *Biochemistry,* **9**, 3243–3248.

Bailey, G. B., Kusamrarn, T. & Vuttivej, K. (1970*b*). Stereospecificity of proton addition to pyridoxal phosphate during transamination catalyzed by dialkylamino acid transaminase. *Fed. Proc. Fed. Amer. Soc. Exp. Biol.* **29**, 857.

Bernstein, F. C., Koetzle, T. F., Williams, G. J. B., Meyer, E. J., Jr, Brice, M. D., Rogers, J. K., Kennard, O., Shimanouchi, T. & Tasumi, M. (1977). The protein data bank: a computer-based archival file for macromolecular structures. *J. Mol. Biol.* **112**, 535–542.

Brändén, C. & Tooze, J. (1991). *Introduction to Protein Structure*, Garland Publishing, New York.

Brückner, H. & Pryzbylski, M. (1984). Isolation and structural characterization of polypeptide antibiotics of the peptaibol class by high performance liquid chromatography with field desorption and fast atom bombardment mass spectrometry. *J. Chromatogr.* **296**, 263–275.

Brünger, A. T. (1990). *XPLOR Manual*, version 2.1, Yale University.

Brünger, A. T., Krukowski, A. & Erickson, J. W. (1990). Slow-cooling for crystallographic refinement by simulated annealing. *Acta Crystallogr. sect A,* **46**, 585–593.

Caffrey, M. S. & Cusanovich, M. A. (1991). Lysines in the amino-terminal α-helix are important to the stability of *Rhodobacter capsulatus* cytochrome *c*2. *Biochemistry,* **30**, 9238–9241.

Christen, P. & Metzler, D. E. (1985). Editors of *Transaminases*, Wiley & Sons, New York.

Corey, E. J. & Sneen, R. A. (1956). Stereoelectronic control in enolization-ketonization reactions. *J. Amer. Chem. Soc.* **78**, 6269–6278.

Cram, D. (1986). Preorganization—from solvents to spherands. *Angew. Chem. Int. Ed. Engl.* **25**, 1039–1057.

Cronin, C. N. & Kirsch, J. F. (1988). Role of arginine-292 in the substrate specificity of aspartate aminotransferase as examined by site-directed mutagenesis. *Biochemistry*, **27**, 4572–4579.

Dunathan, H. C. (1966). Conformation and reaction specificity in pyridoxal phosphate enzymes. *Proc. Nat. Acad. Sci., U.S.A.* **55**, 712–716.

Eijsink, V. G., Vriend, G., van den Burg, B., van der Zee, J. R. & Venema, G. (1992). Increasing the thermostability of a neutral protease by replacing positively charged amino acids in the N-terminal turn of α-helices. *Protein Eng.* **5**, 165–170.

Fersht, A. (1985). *Enzyme Structure and Mechanism*. Freeman, New York.

Ford, G. C., Eichele, G. & Jansonius, J. N. (1980). Three-dimensional structure of a pyridoxal phosphate dependent enzyme, mitochondrial aspartate aminotransferase. *Proc. Nat. Acad. Sci., U.S.A.* **77**, 2559–2563.

Gallagher, T., Snell, E. E. & Hackert, M. L. (1989). Pyruvoyl-dependent histidine decarboxylase. Active site structure and mechanistic analysis. *J. Biol. Chem.* **264**, 12737–12743.

Glusker, J. P. (1991). Structural aspects of metal liganding to functional groups in proteins. *Advan. Protein Chem.* **42**, 1–76.

Goldberg, J. M., Swanson, R. V., Goodman, H. S. & Kirsch, J. F. (1991). The tyrosine 225 to phenylalanine mutation of *Escherichia coli* aspartate aminotransferase results in an alkaline transition in the spectrophotometric and kinetic pK_a values and reduced values of both k_{cat} and K_m. *Biochemistry,* **30**, 305–312.

Gros, P., Kalk, K. H. & Hol, W. G. (1991). Calcium binding to thermitase. Crystallographic studies of thermitase at 0, 5, and 100 mM calcium. *J. Biol. Chem.* **266**, 2953–2961.

Gursky, O., Li, Y., Badger, J. & Caspar, D. L. (1992). Monovalent cation binding to cubic insulin crystals. *Biophys. J.* **3**, 604–611.

Hohenester, E., Keller, J. W. & Jansonius, J. N. (1994). An alkali metal ion size-dependent switch in the active site structure of dialkylglycine decarboxylase. *Biochemistry,* in the press.

Hol, W. G. (1985). The role of the α-helix dipole in protein function and structure. *Progr. Biophys. Mol. Biol.* **45**, 149–195.

Honma, M., Ikeda, M. & Shimomura, T. (1972). Aminotransferase activity of α-aminoisobutyric acid decomposing enzyme. *Agr. Biol. Chem. (Tokyo)* **36**, 1661–1666.

Hurley, J. H. & Remington, S. J. (1992). Contribution of charged side chains, Mg^{2+}, and solvent exclusion to enzymatic β-decarboxylation of α-keto acids. *J. Amer. Chem. Soc.* **114**, 4769–4773.

Hyde, C. C., Ahmed, S. A., Padlan, E. A., Miles, E. W. & Davies, D. R. (1988). Three-dimensional structure of the tryptophan synthetase $\alpha_2\beta_2$ multienzyme complex from *Salmonella typhimurium*. *J. Biol. Chem.* **263**, 17857–17871.

Jäger, J (1991). Crystallographic studies of wild type and mutant aspartate aminotransferase from *Escherichia coli.* Doctoral thesis, University of Basel, Switzerland.

Jansonius, J. N. & Vincent, M. G. (1987). Structural basis for catalysis by aspartate aminotransferase. In *Biological Macromolecules & Assemblies* (Jurnak, F. A., & McPherson, A., eds), vol. 3, pp. 187–288, Wiley & Sons, New York.

Jones, T. A. & Thirup, S. (1986). Using known substructures in protein model building and crystallography. *EMBO J.* **5**, 819–822.

Jones, T. A., Zou, J.-Y., Cowan, S. W. & Kjeldgaard, M. (1991). Improved methods for building protein models in electron density maps and the location of errors in these models. *Acta Crystallogr. sect. A*, **47**, 110–119.

Julin, D. A. & Kirsch, J. F. (1989). Kinetic isotope effects on asparate aminotransferase: evidence for a concerted 1,3 prototropic shift mechanism for the cyosolic isozyme and L-aspartate and dichotomy in mechanism. *Biochemistry*, **28**, 3825–3833.

Kabsch, W. (1988). Evaluation of single crystal X-ray diffraction data from a position sensitive area detector. *J. Appl. Crystallogr.* **21**, 916–924.

Kabsch, W. & Sander, C. (1983). Dictionary of protein secondary structure: pattern recognition of hydrogen bonded and geometrical features. *Biopolymers*, **22**, 2577–2637.

Kalyankar, G. D. & Snell, E. E. (1962). Pyridoxal-catalyzed decarboxylation of amino acids. *Biochemistry*, **1**, 594–600.

Keller, J. W., Baurick, K. B., Rutt, G. C., O'Malley, M. V., Sonafrank, N. L., Reynolds, R. A., Ebbesson, L. O. E. & Vajdos, F. F. (1990). *Pseudomonas cepacia* 2,2-dialkylglycine decarboxylase. Sequence and expression in *Escherichia coli* of structural and repressor genes. *J. Biol. Chem.* **265**, 5531–5539.

Kirsch, J. F., Eichele, G., Ford, G. C., Vincent, M. G., Jansonius, J. N., Gehring, H. & Christen, P. (1984). Mechanism of action of aspartate aminotransferase proposed on the basis of its spatial structure. *J. Mol. Biol.* **174**, 497–525.

Kooystra, P. J., Kalk, K. H. & Hol, W. G. J. (1988). Soaking in Cs_2SO_4 reveals a caesium-aromatic interaction in bovine-liver rhodanese. *Eur. J. Biochem.* **177**, 345–349.

Lamartiniere, C. A., Itoh, H. & Dempsey, W. B. (1971). α-Dialkylamino acid transaminase from *Pseudomonas cepacia*. Purification, crystallization, physical, and kinetic properties. *Biochemistry*, **10**, 4783–4788.

Leslie, A. G. W. (1987) A reciprocal space method for calculating a molecular envelope using the algorithm of B. C. Wang. *Acta Crystallogr. sect. A*, **43**, 134–136.

Leslie, A. G. W., Brick, P. & Wonacott, A. J. (1986). An improved program package for the measurement of oscillation photographs. *CCP4 News*, **18**, 33–39.

Lewis, C., Paneth, P., O'Leary, M. H. & Hilvert, D. (1993). Carbon kinetic isotope effects on the spontaneous and antibody-catalyzed decarboxylation of 5-nitro-3-carboxybenzisoxazole. *J. Amer. Chem. Soc.* **115**, 1410–1413.

Lijk, L. J., Trofs, C. A., Kalk, K. H., De Maeyer, M. C. H. & Hol, W. G. J. (1984). Differences in the binding of sulfate, selenate and thiosulfate ions to bovine liver rhodanese, and a description of a binding site for ammonium and sodium ions. An X-ray diffraction study. *Eur. J. Biochem.* **142**, 399–408.

Luzzati, V. (1952). Traitement statistique des erreurs dans la determination des structures cristallines. *Acta Crystallogr. sect. A*, **5,** 802–810.

Marlier, J. F. & O'Leary, M. H. (1986). Solvent dependence of the carbon kinetic isotope effect on the decarboxylation of 4-pyridylacetic acid. A model for enzymatic decarboxylation. *J. Amer. Chem. Soc.* **108**, 4896–4899.

McPhalen, C. A., Strynadka, N. C. J. & James, M. N. G. (1991). Calcium binding sites in proteins: a structural perspective. *Advan. Protein Chem.* **42**, 77–144.

McPhalen, C. A., Vincent, M. G., Picot, D., Jansonius, J. N., Lesk, A. M. & Chothia, C. (1992*a*). Domain closure in mitochondrial aspartate aminotransferase. *J. Mol. Biol.* **227**, 197–213.

McPhalen, C. A., Vincent, M. G. & Jansonius, J. N. (1992*b*). X-ray structure refinement and comparison of three forms of mitochondrial aspartate aminotransferase. *J. Mol. Biol.* **225**, 495–517.

Mehta, P. K., Hale, T. I. & Christen, P. (1989). Evolutionary relationships among aminotransferases. *Eur. J. Biochem.* **186**, 249–253.

Mehta, P. K., Hale, T. I. & Christen, P. (1993). Aminotransferases: demonstration of homology and division into evolutionary subgroups. *Eur. J. Biochem.* **214**, 549–561.

Messerschmidt, A. & Pflugrath, J. W. (1987). Crystal orientation and X-ray pattern prediction routines for area-detector diffraction systems in macromolecular crystallography. *J. Appl. Crystallogr.* **20**, 306–315.

Morris, A. L., MacArthur, M. W., Hutchinson, E. G. & Thornton, J. M. (1992). Stereochemical quality of protein structure coordinates. *Proteins: Struct. Funct. Genet.* **12**, 345–364.

Muirhead, H. (1987). Pyruvate kinase. In *Biological Macromolecules and Assemblies* (Jurnak, F. A. & McPherson, A., eds), vol. 3, pp. 143–186, Wiley Interscience, New York.

Nicholson, H., Anderson, D. E., Dao-pin, S. & Matthews, B. W. (1991). Analysis of the interaction between charged side chains and the α-helix dipole using designed thermostable mutants of phage T4 lysozyme. *Biochemistry*, **30**, 9816–9828.

Pantoliano, M. W., Whitlow, M., Wood, J. F., Rollence, M. L., Finzel, B. C., Gilliland, G. L., Poulos, T. L. & Bryan, P. N. (1988). The engineering of binding affinity at metal ion binding sites for the stabilization of proteins: subtilisin as a test case. *Biochemistry*, **27**, 8311–8317.

Pascarella, S., Schirch, V. & Bossa, F. (1993). Similarity between serine hydroxymethyltransferase and other pyridoxal phosphate-dependent enzymes. *FEBS Letters*, **331**, 145–149.

Priestle. (1988). RIBBON: a stereo cartoon drawing program for proteins. *J. Appl. Crystallogr.* **21,** 572–576.

Read, R. J. (1986). Improved Fourier coefficients for maps using phases from partial structures with errors. *Acta Crystallogr. sect. A*, **42**, 140–149.

Severin, E., Gulyaev, N., Khurs, E. & Khomutov, R. (1969). The synthesis and properties of phosphopyridoxyl amino acids. *Biochem. Biophys. Res. Commun.* **35**, 318–323.

Sukhareva, B. (1986). Amino acid decarboxylases. In *Vitamin B_6. Chemical, Biochemical, and Medical Aspects* (Dolphin, D., Poulson, R., & Avramovic, O., eds), part B, pp. 325–353, Wiley Interscience, New York.

Thaller, C., Weaver, L. H., Eichele, G., Wilson, E., Karlsson, R. & Jansonius, J. N. (1981). Repeated seeding technique for growing large single crystals of proteins. *J. Mol. Biol.* **147**, 465–469.

Toney, M. D. & Kirsch, J. F. (1989). Direct Bronsted analysis of the restoration of activity to a mutant enzyme by exogenous amines. *Science*, **243**, 1485–1488.

Toney, M. D. & Kirsch, J. F. (1991). Kinetics and equilibria for the reactions of coenzymes with wild type and the Y70F mutant of *Escherichia coli* aspartate aminotransferase. *Biochemistry*, **30**, 7461–7466.

Toney, M. D. & Kirsch, J. F. (1993). Lysine 258 in aspartate aminotransferase: enforcer of the circe effect for amino acid substrates and general-base catalyst for the 1,3-prototropic shift. *Biochemistry*, **32**, 1471–1479.

Toney, M. D., Keller, J. W., Pauptit, R. A., Jaeger, J., Wise, M. K., Sauder, U. & Jansonius, J. N. (1991). Crystallization and preliminary X-ray diffraction studies of dialkylglycine decarboxylase, a decarboxylating transaminase. *J. Mol. Biol.* **222**, 873–875.

Toney, M. D., Hohenester, E., Cowan, S. W. & Jansonius, J. N. (1993). Dialkylglycine decarboxylase structure: bifunctional active site and alkali metal sites. *Science*, **261**, 756–759.

Tronrud, D. E., Ten Eyck, L. F. & Matthews, B. W. (1987). An efficient general purpose least-squares refinement program for macromolecular structures. *Acta Crystallogr. sect. A*, **43**, 489–501.

Wang, B. C. (1985). Resolution of phase ambiguity in macromolecular crystallography. *Methods Enzymol.* **115**, 90–112.

Watanabe, N., Sakabe, K., Sakabe, N., Higashi, T., Sasaki, K., Aibara, S., Morita, Y., Yonaha, K., Toyama, S. & Fukutani, H. (1989). Crystal structure analysis of ω-amino acid:pyruvate aminotransferase with a newly developed Weissenberg camera and an imaging plate using synchrotron radiation. *J. Biochem.* **105**, 1–3.

Watanabe, N., Yonaha, K., Sakabe, K., Sakabe, N., Aibara, S. & Morita, Y. (1991). Crystal structure of ω-amino acid:pyruvate aminotransferase. In *Enzymes Dependent on Pyridoxal Phosphate and Other Carbonyl Compounds as Cofactors* (Fukui, T., Kagamiyama, H., Soda, K. & Wada, H., eds), pp. 121–124, Pergamon Press, Oxford.

Yano, T., Kuramitsu, S., Tanase, S., Yoshimasa, M., Hiromi, K. & Kagamiyama, H. (1991). The role of His143 in the catalytic mechanism of *Escherichia coli* aspartate aminotransferase. *J. Biol. Chem.* **266**, 6079–6085.

Yano, T., Kuramitsu, S., Tanase, S., Morino, Y. & Kagamiyama, H. (1992). Role of Asp222 in the catalytic mechanism of *Escherichia coli* aspartate aminotransferase. *Biochemistry*, **31**, 5878–5887.

Yonaha, K., Nishie, M. & Aibara, S. (1992). The primary structure of ω-amino acid:pyruvate aminotransferase. *J. Biol. Chem.* **267**, 12506–12510.

Edited by R. Huber

(Received 28 July 1994; accepted 30 September 1994)